Progress toward redetermining the Boltzmann constant with a fixed-path-length cylindrical resonator

J. T. Zhang[1*], H. Lin[1], X. J. Feng[1], J. P. Sun[1], K. A. Gillis[2], M. R. Moldover[2], Y. Y. Duan[3]

[1]National Institute of Metrology, Beijing 100013, China

[2]National Institute of Standards and Technology, Gaithersburg, MD 20899-8360, USA

[3]Tsinghua University, Beijing 100084, China

Abstract:

We used a single, fixed-path-length cylindrical-cavity resonator to measure c_0 = (307.8252 ± 0.0012) m·s^{-1}, the zero-density limit of the speed of sound in pure argon at the temperature of the triple point of water. Three even and three odd longitudinal modes were used in this measurement. Based on the ratio M/γ_0 = (23. 968 644 ± 0. 000 033) g·mol^{-1}, determined from an impurity and isotopic analysis of the argon used in this measurement and our measured c_0, we obtain the value k_B = 1.380 650 6×10^{-23} J·K^{-1} for the Boltzmann constant. This value of k_B has the relative uncertainty $u_r(k_B)$ = 7.6×10^{-6} and is fractionally, $(0.12 \pm 7.8)\times10^{-6}$ larger than the value recommended by CODATA in 2006. (The uncertainty is one standard uncertainty.) Several, comparatively large imperfections of our prototype cavity affect the even longitudinal modes more than the odd modes. Our models for these imperfections are approximate, but they suggest that an improved cavity will significantly reduce the uncertainty of c_0.

* Author to whom any correspondence should be addressed, Email: zhangjint@nim.ac.cn

1. Introduction

The Boltzmann constant k_B relates the thermodynamic temperature to thermal energy. Today, the kelvin is defined such that the thermodynamic temperature of the triple point of water T_{TPW} is exactly 273.16 K. As part of a larger change to the International System of Units (SI), Mills et al. [1] propose to replace the present definition of the kelvin with a new one that specifies an exact value of k_B. The specified value of k_B will be chosen to agree with the best measurements available.

Since the 1970s, acoustic resonators have been the preferred method for determining k_B [2,3,4,5,6,7,8,9], thermodynamic temperatures [10,11,12,13,14], and the thermophysical properties of gases. For determining k_B, acoustic resonators rely on kinetic theory to relate the speed of sound in a dilute monatomic gas to the kinetic energy of the gas atoms and, therefore, to the thermodynamic temperature. For the highest possible accuracy, acoustic resonance measurements in dilute gases use non-degenerate modes, which are the radially-symmetric modes in a spherical or quasi-spherical cavity and the longitudinal modes in a cylindrical cavity. Among these modes, the radial modes of spherical and quasi-spherical resonators have the advantage of high quality factors, Qs. For resonators of the same volume, the Qs of the low-frequency radially-symmetric modes of a spherical cavity are 5 times larger than the Qs of low-frequency longitudinal modes of a cylindrical cavity. Despite this significant advantage of spherical and quasi-spherical resonators, we chose to use the non-degenerate longitudinal modes of a fixed-path-length cylindrical resonator to re-determine k_B. In part, our choice was motivated by the recommendation of the Consultative Committee of Thermometry (CCT) that the redefinition of the kelvin should be based on three different methods of measuring k_B. In common with several other recent measurements of k_B, we used an argon-filled acoustic cavity resonator; however, the corrections to measured resonance frequencies required to determine the thermodynamic speed of sound are quite different for spherical and cylindrical cavities. Furthermore, we have measured the length of our cylindrical cavity using two-color optical interferometry. Interferometry is subject to very different errors than either pychnometry or microwave dimensional metrology, the two methods that have been used to determine the volume of spherical and quasi-spherical cavities.

In this publication, we summarize our measurements of the acoustic resonance frequencies, the length of the cylindrical cavity, the impurities and isotopic abundances of the argon, and the argon's temperature. (Part of this work was published previously [9,15,16,17].) We also describe the corrections to the acoustic frequencies and the determination of k_B from fits of the frequencies by a physically motivated function of the pressure. Our principal result is: $k_B = (1.380\,650\,6 \pm 0.000\,010\,5)\times10^{-23}$ J·K^{-1}. This new value of k_B has the relative standard uncertainty $u_r(k_B) = 7.6\times10^{-6}$; it is, fractionally, 0.12×10^{-6} larger than the value recommended in CODATA 2006 [18] and 0.30×10^{-6} larger than Moldover et al.'s measurement in 1988 [3]. It is also consistent with the recent determinations of k_B using quasi-spherical cavities [5,6,7]. Our analysis also determined the second acoustic virial coefficient of argon at T_{TPW}: $\beta_a = (5.34 \pm 0.15)\ \mathrm{cm^3\ mol^{-1}}$. This result is also consistent with the values obtained using spherical and quasi-spherical resonators [3,11,5,6,7,19,20,21,22].

The uncertainty of our value of k_B is dominated by the 6 inconsistent values of k_B determined by the data for each of 3 even and 3 odd longitudinal acoustic modes of our cavity resonator. The inconsistencies may originate in our limited ability to characterize and model the differences between the actual cavity and a perfect circular cylinder. For example, the fill tube that was used to move argon in and out of the cavity had a comparatively large inner diameter and it was surrounded by a gap (slit) where it joined the cavity. We used approximate models to calculate the frequency perturbations produced by these features. The perturbations were comparatively large and sensitive to a poorly-known volume terminating the slit. However, the fill tube and gap joined the cavity at a symmetric location where its effects on the odd longitudinal modes were small. Therefore, we assessed possible effects of the approximations by calculating another value of k_B using only the odd longitudinal modes. This value was, fractionally, $(5.0 \pm 5.2)\times10^{-6}$ larger than the CODATA value. This suggests that, elimination of the gap and similar modifications of cavity might reduce the uncertainty of our results by a factor of two or more.

2. Fundamentals of measurement

2.1 Thermodynamic relation

The Boltzmann constant k_B is related to the speed of sound in an ideal gas by:

$$k_{\mathrm{B}} = \frac{c_0{}^2 M}{T\gamma_0 N_{\mathrm{A}}} \quad , \tag{1}$$

where c_0 denotes the speed of sound at the thermodynamic temperature T; N_A is the Avogadro constant; M is the molar mass of the working gas; $\gamma_0 \equiv C_P/C_V$ is the ratio of the specific heat capacities that has the value 5/3 for ideal monatomic gases. The uncertainty of the Avogadro constant is 5×10^{-8} which is two orders of magnitude smaller than the uncertainty of k_B. [18] Therefore, we consider N_A to be known.

The resonance frequencies f_l^0 of the longitudinal acoustic modes (l00) of a gas-filled, geometrically-perfect, rigid, perfectly-thermally-insulating, cylindrical cavity are determined by the speed of sound in the gas c and the length L of the cavity by the formula

$$f_l^0 = \frac{lc}{2L} \tag{2}$$

where $l = 0,1, 2,\ldots$ is the longitudinal mode index [9]. (Since this work focuses on pure longitudinal modes, we refer to these modes using only the longitudinal index l in subscripts for convenience. Other types of modes are designated by the complete triplet of indices.) Upon combining this formula with Eq. (1) we obtain the relation between k_B and the acoustic resonance frequencies of an idealized, gas-filled cavity

$$k_B = \left(\frac{2f_l^0 L}{l}\right)^2 \frac{M}{T\gamma_0 N_A} \quad . \tag{3}$$

Our cavity had a radius $a \approx 40$ mm, a length $L \approx 130$ mm and we used the modes $l = 2, 3, \ldots, 7$. The resonance frequencies ranged from 2.4 kHz to 8.3 kHz.

2.2 Perturbations to the Resonance Frequencies

The perturbations to the ideal resonance frequencies f_l^0 caused by imperfect geometry and other well-understood physical phenomena have been described in our previous publications [9,15]. For completeness, we review these perturbations here.

2.2.1 Boundary layers

The non-zero thermal and viscous admittances of the solid shell surrounding the cavity cause the measured resonance frequencies to differ from their unperturbed values. The acoustic oscillations are subject to viscous damping in the boundary layer where the gas is in contact with the surrounding shell. For the longitudinal modes, the viscous damping adds to the ideal resonance frequency the term $(\Delta f_l)_\mathrm{v}$

$$\frac{(\Delta f_l)_\mathrm{v}}{f_l^0} = -\frac{1}{2a}\left(\delta_\mathrm{v} - 2l_\mathrm{v}\right) \quad . \tag{4}$$

Here, a denotes the radius of the cylindrical cavity; l_v denotes the pressure-dependent viscous accommodation length; δ_v is the viscous penetration length defined by

$$\delta_\mathrm{v} = \sqrt{\frac{\eta}{\pi f \rho}} \quad . \tag{5}$$

Here, f denotes the measured resonance frequency and η and ρ are the viscosity and mass density, respectively, at the working temperature and pressure. The viscous accommodation length is given by

$$l_\mathrm{v} = \frac{\eta}{p}\sqrt{\frac{\pi RT}{2M}}\frac{2-h_\mathrm{v}}{h_\mathrm{v}} \quad . \tag{6}$$

Here, $R \equiv k_\mathrm{B}N_\mathrm{A}$ is the universal gas constant, and h_v is the viscous (or momentum) accommodation coefficient which has a value near 1. [23] The viscous boundary layer also increases the half-widths $(g_l)_\mathrm{v}$ of acoustic resonances by [17]

$$\frac{(g_l)_\mathrm{v}}{f_l^0} = -\frac{(\Delta f_l)_\mathrm{v}}{f_l^0} = \frac{\delta_\mathrm{v}}{2a} = \frac{1}{2a}\sqrt{\frac{\eta}{\pi f \rho}} \quad . \tag{7}$$

The irreversible heat exchange between the gas oscillating in the cavity and the shell surrounding the cavity adds to the ideal resonance frequencies the term $(\Delta f_l)_{\text{th}}$

$$\frac{(\Delta f_l)_{\text{th}}}{f_l^0} = -\frac{\gamma-1}{2a}\left[\left(\delta_{\text{th}} - 2l_{\text{th}}\right)\left(1+\frac{2a}{L}\right) - \frac{\lambda}{\lambda_{\text{shell}}}\delta_{\text{th,shell}} - \frac{2a}{L}\frac{\lambda}{\lambda_{\text{endplate}}}\delta_{\text{th,endplate}}\right] \quad . \quad (8)$$

Here, $\gamma \equiv C_P/C_V$ is the adiabatic index, in which C_P and C_V are the constant-pressure and constant-volume specific heats at the working temperature and pressure. δ_{th} is the thermal penetration length that characterizes the penetration of the thermal boundary layer from the cavity's wall into the gas

$$\delta_{\text{th}} = \sqrt{\frac{\lambda}{\pi f \rho C_P}} \quad . \quad (9)$$

Here, λ denotes thermal conductivity of the gas at the working temperature and pressure. In Eq. (8), the subscripts "shell" and "endplate" indicate properties of the material.

In Eq. (8), l_{th} denotes the thermal accommodation length, given by [3]

$$l_{\text{th}} = \frac{\lambda}{p}\sqrt{\frac{\pi MT}{2R}}\frac{2-h_{\text{th}}}{h_{\text{th}}}\frac{1}{C_{V,m}/R + 0.5} \quad , \quad (10)$$

where h_{th} is the thermal accommodation coefficient that has been found to be approximately 1.0 for several acoustic resonators [3,11], $C_{V,m}$ is the molar specific heat at constant volume of the gas. At low gas pressures, the frequency perturbations terms $(\Delta f_l)_{\text{v}}$ and $(\Delta f_l)_{\text{th}}$ increase as (pressure)$^{-1}$ as the pressure is reduced. In the discussion below, we allow for this dependence in the determination of the zero-pressure speed of sound c_0 by correcting the measured resonance frequencies for known effects and then fitting the corrected frequencies by a polynomial function of the pressure with and without a p^{-1} term.

The irreversible heat exchange between the gas oscillating in the cavity and the shell increases the half-widths of the acoustic resonances by the term $(g_l)_{\text{th}}$:

$$\frac{(g_l)_{\text{th}}}{f_l^0} = \frac{\gamma-1}{2a}\left[\delta_{\text{th}}\left(1+\frac{2a}{L}\right) - \frac{\lambda}{\lambda_{\text{shell}}}\delta_{\text{th,shell}} - \frac{2a}{L}\frac{\lambda}{\lambda_{\text{endplate}}}\delta_{\text{th,endplate}}\right] \quad . \quad (11)$$

Acoustic oscillations are attenuated throughout the volume of the cavity by both the viscosity and the thermal conductivity of the gas. This attenuation contributes a term to the resonance half-width [3] given by the term $(g_l)_{\mathrm{bulk}}$:

$$\frac{(g_l)_{\mathrm{bulk}}}{f_l^0}=\left(\frac{\pi f}{c}\right)^2\left[\frac{4}{3}\delta_{\mathrm{v}}^2+(\gamma-1)\delta_{\mathrm{th}}^2\right] \quad . \tag{12}$$

2.2.2 Mechanical admittance of the shell

The shell surrounding the cavity deforms in response to the acoustic pressure in the gas. In general, the mechanical admittance associated with these deformations is difficult to calculate. In a prior publication [9], we calculated perturbations for three deformations: (1) radial ($\Delta f_{\mathrm{sh},1}$) and (2) axial ($\Delta f_{\mathrm{sh},2}$) deformations of a finite-length cylindrical shell, and (3) bending of the end-plates ($\Delta f_{\mathrm{sh},3}$). These perturbations have similar functional forms

$$\frac{(\Delta f_l)_{\mathrm{sh},i}}{f_l^0}\approx-\left(\rho c^2\right)_{\mathrm{gas}}\frac{G_{i,l}}{1-\left(f_l^0/f_{\mathrm{sh},i}\right)^2} \quad , \tag{13}$$

where the compliance $G_{i,l}$ depends upon the geometry, the gas mode l, and elastic properties of the resonator and $f_{\mathrm{sh},i}$ is the frequency of the i^{th} resonance of the shell for the deformation under consideration. For the present resonator, our estimates are: (1) for radial motion, $f_{\mathrm{sh},1}$ ≈ 20.23 kHz for l = 2,4,6 and 26.85 kHz for l = 3,5,7. The scaled compliances $G_{i,l}^*\equiv 10^{12}\,\mathrm{J{\bullet}m^{-3}}G_{i,l}$ are $G_{1,2}^*$ through $G_{1,7}^*$ are 1.91, 1.23, 0.559, 0.268, 0.136, 0.0767, respectively. (2) For axial motion, $f_{\mathrm{sh},2}$ ≈ 15.1 kHz and G_2^* = 4.23 and, (3) for the bending of the end-plates assuming that both plates were simply supported around their average circumference $f_{\mathrm{sh},3}$ ≈ 12.6 kHz and G_3^* = 2.67; for bending of the end-plates assuming that both plates were clamped to a rigid cylinder, $f_{\mathrm{sh},3}$ ≈ 27.1 kHz and G_3^* = 4.36.

For the acoustic modes with odd l, the unbalanced acoustic pressure on the end-plates causes recoil. For simplicity, we estimated the recoil perturbation by approximating the steel cylinder as a rigid, free body. In this approximation, the perturbation is

$$\frac{\left(\Delta f_l\right)_{\text{sh4}}}{f_l^0} = -\frac{1}{2}\frac{KE_{\text{solid}}}{KE_{\text{fluid}}} = -\left(\frac{2}{l\pi}\right)^2 \frac{M_{\text{gas}}}{M_{\text{res}}}, \text{odd } l \quad , \tag{14}$$

where the last equality is in terms of the total mass of the gas M_{gas} ($\approx$ 0.0011 kg at 100 kPa) and the mass of the resonator M_{res}.$\approx$ 12 kg. When we measured k_B, the cylindrical resonator was clamped to a stage that was bolted to the pressure vessel which was hung inside the thermostat. This assembled structure had its own mechanical resonance frequencies. In the unlikely circumstance that all of these frequencies were above the frequencies of the (l00) modes (1.2 kHz to 8.3 kHz), M_{res} in Eq. (14) should be replaced with the larger mass $M_{\text{assembly}} \approx 180$ kg.

Significantly, all four perturbations from the shell's admittance $\Delta f_{\text{sh},i}$ have a nearly linear dependence on the pressure of the gas. As discussed in Section 5.6, we deduce k_B by correcting the measured resonance frequencies for the known perturbations and fitting the corrected resonance frequencies to polynomial functions of the pressure. Therefore, our imperfect estimates of $\Delta f_{\text{sh},i}$ will lead to mode-dependent values of the second acoustic virial coefficient β_a. However, the imperfect estimates do not affect the values of c_0 and k_B. The expected linear dependence of $\Delta f_{\text{sh},i}$ on the pressure results from three concepts: (1) conservation of momentum, which leads to perturbations in the form of Eq. (13), (2) over the narrow range of our measurements ($T = T_{\text{TPW}}$ and $p < 550$ kPa) the quantity $\rho c^2/p$ changes only 0.6 % and f_l changes only 0.15 %, and (3) $f_l << f_{\text{sh},i}$ from our estimates of the shell resonance frequencies, therefore the denominator in Eq. (13) never gets so close to zero that the pressure dependence of $f_l / f_{\text{sh},i}$ is significant.

2.2.3 Gas fill duct

We used the method of Gillis et al. [15] to calculate the frequency perturbations $(\Delta f_l)_d$ to the (l00) modes caused by the duct that admitted gas into the cavity. The duct opened to the cavity mid-way between the end-plates where the odd (l00) modes have a pressure node. Therefore $(\Delta f_l)_d = 0$ for the odd l modes, in the first order of the theory. We determined the inner diameter of the fill duct by measuring the pressure difference across the ends of the duct while a measured quantity of argon flowed through it. The inner diameter was 2.133 mm ± 0.002 mm and the duct's length was 2.744 m ± 0.005 m. We coiled the duct around the outside of the resonator. At top of the pressure vessel, the fill duct joined a larger tube that had an inner diameter of 4.57 mm, a length of 2 m and was, for most of its length, at ambient temperature. The larger tube led to a diaphragm valve that had a small internal volume and was always closed during the acoustic measurements.

The largest fill-duct perturbations occurred for the (200) mode at 2.4 kHz. These perturbations ranged from $(\Delta f_d + i\Delta g_d)/f = (+0.4 + i116.4)\times10^{-6}$ at 550 kPa to $(\Delta f_d + i\Delta g_d)/f = (-0.8 + i112.4)\times10^{-6}$ at 50 kPa. The large imaginary part of these perturbations is a cause for concern because $\Delta g_{\mathrm{d}}/f \approx (r_{\mathrm{d}}/a)^2/(l\pi)$ sets the scale for acoustic energy in the duct. An un-modeled, pressure-independent mechanism could alter the phase cancellation within the duct and thereby change Δf_d by as much as 1 % of Δg_d. Such a change would generate an error in k_B of 2×10^{-6}. The effect of the uncertainty of the fill duct length was largest for the (200) mode at the highest pressure. A change of ±5 mm in the fill duct length changed the perturbation $(\Delta f_2)_{\mathrm{d}}/f$ by $\pm1.7\times10^{-6}$ at 550 kPa, but did not change the perturbation at 50 kPa. This pressure-dependent sensitivity increases the uncertainty of the determination of c_0^2 for the (200) mode by 1.8×10^{-6}. In the future, we will use a smaller-diameter duct to reduce the perturbations.

2.2.4 Slit surrounding the gas fill duct

Figure 1 displays the entrance of the duct into the cylindrical shell of the resonator. The duct was sealed to the outside of the shell with a commercial compression fitting. To avoid compressing the duct, the fitting was not tightened to the manufacturer's specification and the seal leaked slightly. This arrangement exposed the acoustic field in the cylindrical cavity to a long, narrow gap between the outside of the duct and the hole in the shell. At its widest point, the gap was measured to be 0.03 mm, with a possible range from 0.02 mm to 0.05 mm. The depth of the gap was estimated to be 35 mm. The admittance of the gap does not perturb the modes with odd l because these modes have a pressure node at the entrance to the gap, midway between the end-plates of the resonator.

We estimated the effect of the gap on the resonance frequencies of the even l modes in two ways. In a first approximation, we assumed that the duct was concentric with the hole in the shell, thereby forming an annular gap. We approximated the annular gap as a slit 35 mm deep with a rectangular cross-section 0.015 mm × 10 mm terminated by an infinite acoustic impedance and we used the formulas in Section 5.3 of Mehl *et al*. [24] to calculate the frequency perturbations. At 550 kPa, the perturbations of the l = 2, 4, 6 resonance frequencies are −1.4 ppm, –0.9 ppm, and –0.6 ppm, respectively. In the range 550 kPa to 100 kPa the perturbations are approximately linear functions of the pressure that extrapolate to –0.6 ppm, –0.4 ppm, and –0.4 ppm, respectively, at zero pressure. In the range of our measurements, the rectangular-slit calculation predicts the half-widths of the l = 2, 4, 6 resonances increase by nearly the same amount as their frequencies decrease.

In a second approximation, we assumed that the duct was off center with the hole in the shell, as sketched in the lower-right corner of Fig. 1. We approximated this shape by two rectangular slits 35 mm deep with cross-sections 0.0075 mm × 5 mm and 0.023 mm × 5 mm. At 550 kPa, the perturbations of the l = 2, 4, 6 resonance frequencies were -1.5 ppm, -0.8 ppm, and -0.4 ppm, respectively. Linear extrapolations give zero-pressure perturbations of -0.8 ppm, -0.6 ppm, and -0.5 ppm, respectively. This two-slit model predicts half-widths that are about 20 % larger than the annular gap model.

2.2.5 Angle between end-plates

As discussed in Section 5.1.2, the end-plates of the cavity were tilted at an angle of 37 microradians with respect to each other. In addition, both end-plates might have been tilted by a similar angle θ with respect to the axis of the cylinder. Such a tilt in the endplates leaves the average cavity length unchanged, to first order in $a\theta/L$ and perturbs the resonance frequencies by an amount proportional to $\left(a\theta/L\right)^2$ and was neglected.

2.2.6 Chamfer on corners of cylinder

Often, the machining of cylindrical shells leaves a burr of metal on every corner; subsequent removal of the burr leaves a chamfer. We measured the dimensions of the chamfers on the inner corners of our shell to be (0.028 ± 0.012) mm high and (0.043 ± 0.006) mm wide as sketched in Fig. 1. The chamfers are located at both ends of the cylinder, which are at pressure anti-nodes for all modes. Therefore all of the longitudinal modes are affected by such chamfers. The chamfers at both ends of the shell together increased the cavity's volume by the fraction $2\Delta V_{\text{cham}}/V_{\text{res}} \approx 4.7\times10^{-7}$ and the solid surfaces exposed to the argon increased by $2\Delta S_{\text{cham}} = 34\ \text{mm}^2$. ($\Delta S_{\text{cham}}$ includes contributions from the metal shell and the fused silica end-plates.) We approximated the actual chamfer by a radial slit with the same volume and surface area in order to estimate the specific acoustic admittance. We chose the slit dimensions to be $2t_{\text{slit}}$ = 0.18 mm high and D_{slit} = 0.033 mm deep for our model. For this geometry, the acoustic admittance y_{cham} is given approximately by a lossy planar waveguide terminated by a lossy plate

$$y_{\text{cham}} = y_0 \frac{y_{\text{T}} + y_0 \tanh\left(\Gamma D_{\text{slit}}\right)}{y_0 + y_{\text{T}} \tanh\left(\Gamma D_{\text{slit}}\right)}, \tag{15}$$

where

$$y_0 = \sqrt{\left[1+\left(\gamma-1\right)F_{\text{t,slit}}\right]\left(1-F_{\text{v,slit}}\right)}, \qquad \Gamma D_{\text{slit}} = ikD_{\text{slit}}\sqrt{\frac{1+\left(\gamma-1\right)F_{\text{t,slit}}}{1-F_{\text{v,slit}}}}, \tag{16}$$

$$F_{\text{t,slit}} \equiv \frac{\tanh\left[\left(1+i\right)t_{\text{slit}}/\delta_{\text{t}}\right]}{\left(1+i\right)t_{\text{slit}}/\delta_{\text{t}}}, \qquad F_{\text{v,slit}} \equiv \frac{\tanh\left[\left(1+i\right)t_{\text{slit}}/\delta_{\text{v}}\right]}{\left(1+i\right)t_{\text{slit}}/\delta_{\text{v}}}, \tag{17}$$

and

$$y_{\text{T}} = \frac{1}{2}\left(1+i\right)\left(\gamma-1\right)k\delta_{th}. \tag{18}$$

The perturbation including both chamfers is

$$\frac{\Delta F}{f_l} = \frac{2i}{l\pi^2 a^2} \Delta y_{\text{cham}} \Delta A_{\text{cham}} \cos^2\left(\frac{l\pi z_{\text{cham}}}{L}\right) \tag{19}$$

where the net change in the admittance is $\Delta y_{\text{cham}} \equiv y_{\text{cham}} - y_{\text{T}}$ and ΔA_{cham} is the surface area of the shell that is replaced by the chamfer. For the (200) mode, Eq. (19) predicts $10^6 \Delta F/f_l \approx -0.77 + i0.04$ at 550 kPa and $10^6 \Delta F/f_l \approx -0.77 + i0.01$ at 100 kPa; whereas, the perturbations for the (700) mode are $10^6 \Delta F/f_l \approx -0.72 + i0.11$ at 550 kPa and $10^6 \Delta F/f_l \approx -0.77 + i0.03$ at 100 kPa. The real part of this perturbation is weakly dependent on both the mode and the pressure. In contrast, the contribution to the half-width depends upon mode and pressure through the thermal penetration length δ_{th}. We also modeled the same chamfer by slits with the extreme dimensions of $2t_{\text{slit}}$ = 0.014 mm high by D_{slit} = 0.043 mm deep and $2t_{\text{slit}}$ = 0.028 mm high by D_{slit} = 0.022 mm deep. We used the differences between the results from the models as a measure of the model's uncertainty. Although this perturbation is fairly small, it does not extrapolate linearly with pressure to near zero, and it depends on difficult-to-measure dimensions. In future work, we will avoid chamfers.

3. Transducer perturbation and signal-to-noise ratio

We used piezoelectric transducers (PZTs) to excite and detect the acoustic resonances. In comparison with the small capacitive microphones that are often used in metrological applications of gas-filled acoustic resonators, the PZT driver generates a significantly larger signal and the PZT detector has a much larger capacitance that allowed us to connect the PZT to a remote amplifier with a coaxial cable. (In contrast, triaxial cable with a driven shield must be used with small microphones.) The drive PZT was excited with 7 V (RMS) and it dissipated 1.0 μW at 2 kHz. Under these conditions, the fractional standard deviation of the voltages from a curve fitting was 2.0×10^{-4}, a factor of 7 smaller than we obtained with the capacitor microphones. As a result, we measured the resonance frequencies f_l with the fractional uncertainty of 2.0×10^{-7} when the Q was greater than 600. The response of each PZT was a linear function of the static pressure. This contrasts with the non-linear pressure dependence of the response of the loud speaker that was used to measure k_B in Ref. [2]. We searched for non-linearity in the response of the installed PZTs to the acoustic pressure by exciting the drive PZT with 3.5, 7, and 14 V_{RMS}. The dependence of the acoustic resonant frequencies on the drive voltage was negligible. We reported the performance of the PZTs elsewhere [9,16].

The end-plates of the cylindrical cavity were made of fused-silica to facilitate the measurement of the cavity's length using laser interferometry. We ground a blind hole into the outside-facing surface of each end-plate to form a diaphragm flush with the inside surface, thereby preserving the cylindrical shape of the cavity. (See Fig. 3.) Each diaphragm had a diameter of 10 mm and a thickness of 0.4 mm. Each PZT disk had a diameter of 6.4 mm and a thickness of 0.5 mm. These disks were bonded to the outer surface of a diaphragm with epoxy and each was concentric with the diaphragm. As discussed in [9], the drive PZT was located 25.2 mm from the axis of the cylinder and the detector PZT was on the axis. The driver and the detector were on opposite ends of the cavity; the 13 cm between them reduced crosstalk.

In response to the acoustic pressure in the cavity, the largest bending stress in each diaphragm occurred near its perimeter. Therefore, the low-frequency compliance of the diaphragm was determined by the properties of fused silica and not by the properties of PZT. We modeled each diaphragm as a thin plate clamped around its perimeter and loaded with a 98 mg, the mass of a PZT transducer. The frequency perturbation generated by the compliance of each diaphragm was

$$\frac{\left(\Delta f_l\right)_{\mathrm{tr}}}{f_l^0} = -\frac{1}{16}\frac{\left(\rho c^2\right)_{\mathrm{g}}}{\left(\rho_{\mathrm{FS}} c_{p,\mathrm{FS}}^2\right)}\left(\frac{2a}{L}\right)\left(\frac{a_{\mathrm{dm}}}{a}\right)^3\left(\frac{a_{\mathrm{dm}}}{t_{\mathrm{dm}}}\right)^3\frac{1}{1-\left(f_l^0/f_{\mathrm{dm}}\right)^2} \quad , \quad (20)$$

where the diaphragm's resonance frequency was $f_{\mathrm{dm}} \approx 38$ kHz. (See Figs. 2 and 3 in Ref. [9].) Because Eq. (20) has the same functional form as Eq. (13), the compliance of the {transducer + diaphragm}, like the compliance of the shell, is nearly a linear function of the pressure. Therefore, imperfections in the modeling of Δf_{tr} affect the determination of the second acoustic virial coefficient β_a, but not k_B.

The perturbations from small capacitive microphones are more complicated than Eq. (20), the perturbation from our PZT transducers. When the diaphragm of a microphone is displaced, it compresses the gas in the complicated cavity between the diaphragm and a back-plate. The compression generates restoring and damping forces that are complicated functions of the frequency, pressure and transport properties of the gas.

4. Experimental setup

The experimental setup and the resonator assembly were sketched in Figs. 2 and 3. The pressure vessel containing the resonator assembly was installed in a thermostat that had a stability of better than ± 0.1 mK in 24 hours [9,17]. The temperature of the resonator was measured using three capsule-type standard platinum resistance thermometers (Hart 5686)[1], of diameter 5.5 mm and length 30 mm. These thermometers were installed at the top, the middle and the bottom of the cylinder. We used an ASL F900 bridge to measure ratios of the thermometer resistances to a 100 Ω standard resistor (Tinsley 5685A) that was thermostatted with a stability of ± 1 mK. The sinusoidal acoustic driving voltage was generated by an arbitrary waveform generator (Agilent 33220A) that was locked to a 10 MHz standard signal derived from a GPS clock. A frequency counter (Agilent 53131A) monitored the signal frequency from the waveform generator. The counter verified that frequency stability was better than 0.05×10^{-6} during the measurement of a single mode. The signal from the PZT detector was measured with a two-phase lock-in amplifier (Stanford Research SR830).

At 20 °C, the cylinder bounding the cavity had the nominal length of 129.390 mm,

[1]In order to describe materials and procedures adequately, it is occasionally necessary to identify commercial products by manufacturer's name or label. In no instance does such identification imply endorsement by either China's National Institute of Metrology or the United States' National Institute of Standards and Technology, nor does it imply that the particular product or equipment is necessarily the best available for the purpose.

a diameter of 80 mm, and a thickness of 30 mm. It was made of bearing steel that had a Young's modulus of 210 GPa (somewhat larger than that of stainless steel), a Poisson's ratio of 0.29 and a density of 7800 kg·m^{-3}. Both end-plates had a thickness 20 mm and were fabricated from optical-quality, fused silica with a Young's modulus of 73 GPa, a Poisson's ratio of 0.17 and a density of 2210 kg·m^{-3}. The inner surface of each end-plate was coated with a partially-reflecting metallic film. Both end-plates were bolted tightly to the cylinder. They were installed using an indicating torque wrench to control the tension in each bolt. Each end-plate had a blind hole that had been machined into the outside-facing surface to form an integrated diaphragm flush with the inside surface, thereby preserving the cylindrical shape of the cavity. As indicated above, the PZT was cemented to the outside surface of each diaphragm with epoxy.

An absolute pressure gauge (Ruska 7250 xi, 0 to 600 kPa) was used to control and measure the argon gas pressure inside the pressure vessel at 50 Pa to 200 Pa below the pressure in the cylindrical cavity. We relied on the flatness of the surfaces of the end-plates and the cylinder's ends to minimize the leakage of the pure argon gas from the cavity into the pressure vessel. These precautions ensured that the argon inside the cavity would not be contaminated by outgassing from the transducers, epoxy, wire insulation, *etc*. in the pressure vessel. A differential pressure gauge (MKS Baratron 616A, 100 Torr) measured the pressure difference between the cavity and a buffer volume thermostatted near ambient temperature. The metal diaphragm of the differential pressure gauge isolated the cavity from the rest of the gas manifold. The pressure inside the buffer volume was measured by another Ruska 7250 xi absolute pressure gauge. The absolute pressure gauge and the differential pressure gauge were calibrated by the National Institute of Metrology (NIM), China. The pressure uncertainty was estimated to be less than ±20 Pa including the uncertainty of the absolute pressure gauge of ±15 Pa from (0 to 600) kPa and the uncertainty of the differential pressure gauge of ±0.12% of reading. The pressure uncertainty contributes no more than 0.05×10^{-6} to the uncertainty in k_B.

5. Measurement Procedures

5.1 Cylinder length measurement

We determined the internal length of the cylindrical cavity in 6 steps. First, we used a coordinate measuring machine to make a comparatively crude measurement of the length of the bearing steel cylinder at 20°C. (Sec. 5.1.1.) Second, we bolted the endplates to the cylinder and used two-color interferometry to make an accurate measurement of the assembled resonator's internal length along an axis displaced 15 mm from the symmetry axis. (Sec. 5.1.2) Third, we rotated the resonator about its symmetry axis while monitoring the interference pattern to determine the angle between the endplates and to determine the length of the cavity on the symmetry axis. (Sec. 5.1.3) Fourth, we measured the thermal contraction of the length as the cavity was cooled to T_{TPW}. Fifth, we estimated the pressured dependence of the length (Sec. 5.1.4) and the effect of bolting the endplates to the cylinder (Sec. 5.1.5). Finally, we estimated the difference between the optical length of the cavity and the acoustical length.

5.1.1 Coordinate measurements of the cylinder's length

Before the conducting the length measurements, we cleaned the bearing steel cylinder to remove the rust-inhibiting oil. Then, it was allowed to thermally equilibrate in the length gauge laboratory for more than 24 hours. The temperature inside the laboratory was controlled within ± 0.2°C. The cylinder was supported horizontally on a 3-dimensional coordinate measuring machine (3D CMM) that was equipped with an integrated laser interferometer. Translational displacements measured with the interferometer reduce the effects of thermal non-uniformities and guiding deviations in the pitch and torsional motion along the CMM. The CMM/laser interferometer was used to determine the distance between 191 pairs of points on the opposite ends of the cylinder. As discussed in Section 5.1.3, we assumed that the ends of the cylinder were non-parallel planes. The result for the average mechanical length of the cylinder's axis was $L_{\mathrm{mech}}(20°\mathrm{C},\ 100\ \mathrm{kPa}) \approx (129.3927 \pm 0.0008)\ \mathrm{mm}$. The uncertainty is one standard uncertainty but does not enter into the uncertainty budget for the determination of k_B.

5.1.2 Two color measurements of the resonator's length

The two end-plates of optical-quality fused silica glass were bolted to the cylinder cavity to form the resonator. The inner surface of each end-plate had been coated with a metallic film to increase its optical reflectivity. As stated in Refs. [25,26], the penetration of laser beams into the partially reflecting films was on the order of 20 nm. The resonator was tightly clamped to a rotation stage inside the pressure vessel, where, as indicated in Fig. 3, the axis of the resonator was vertical. The pressure vessel assembly, together with the rotation stage and the resonator inside it, was maintained in the laboratory at (20.0±0.2)°C.

The resonator was filled with argon at the pressure 101.603 kPa. The temperature of the argon was monitored using the thermometers installed in the walls bounding the cavity and averaged 19.916 °C with fluctuations of 0.002 °C. We adopted the values of the refractive index of argon from Ref. [27] and we corrected them for small density changes using the suitable approximation: $\rho_2(n_1^2-1)=\rho_1(n_2^2-1)$.

In our previous publication [9], we described the use of two-color interferometry to determine the length of the cylindrical cavity. Our analysis follows Ref. [28] and uses measurements of fractional interference fringes formed by two lasers of known, unequal wavelengths. Our lasers had nominal wavelengths of 633 nm and 543 nm and beam diameters of approximately 1 mm. Both lasers were calibrated and had a fractional stability better than 2×10^{-8}. As sketched in Fig. 3, the laser beams entered the vertical cavity through the top end-plate and exited through the bottom end-plate onto a camera. The laser beams formed two sets of equal-inclination interference patterns because of the ≈ 37 microradian angle that existed between the metallic films when the end-plates were bolted to the cylinder. From measurements of the fractional fringes, we determined the optical length of between the windows with an uncertainty of 30 nm, which contributed a standard relative uncertainty of 0.46×10^{-6} to the determination of k_B.

5.1.3 Angle between end-plates

As shown in Fig. 4 of Ref. [9], one acoustic transducer was located on the axis of the resonator and the other was located, radially, 25.2 mm off of the axis. To avoid the transducers, the laser beams entered the cavity parallel to its axis but approximately 15 mm from the axis. Because the laser measurements were made off-axis and because there was an angle between the end-plates, the length determined by the laser measurements had to be corrected to determine the cavity's length on its axis. (It is the axial length that determines the frequencies of the (l00) acoustic modes.) To determine the correction, we rotated the resonator about its axis and observed the interference fringes first expand outward and then contract inward, finally returning to their initial positions when a full rotation was completed. These observations indicated that, by accident, the laser measured the shortest length on the 15 mm radius. The displacement of the 633 nm laser fringes was measured and interpreted by assuming that the metallic reflecting film on each end-plate was flat and rigid. The total variation of cylinder length was 1.143 μm and the length of the cavity's axis (the arithmetic mean length) was 0.572 μm larger than that measured by two color laser interferometry at the original orientation. We concluded that the mean optical length of the cavity was L_{opt}(19.916 °C, 101.604 kPa) = (129.39 171 ± 0.00 003) mm.

5.1.4 Thermal contraction

The pressure vessel, together with the rotation stage and the resonator inside it, were cooled from an initial equilibrium state at 19.9165°C and 101.603 kPa to a final equilibrium state at T_{TPW} and 94.921 kPa. The resonator's contraction between these equilibrium states was calculated by counting interference fringes, measuring the initial and final fringe fractions, and accounting for the small (0.45×10^{-6}) fractional increase of the refractivity of argon in the cavity as the density of the argon in the cavity increased. As the cooling proceeded, we continuously recorded the CCD images of the interference fringes from the 633 nm laser as well as the pressure in the cylinder and the readings of the thermometers embedded in the cylinder. During the cooling process, valve V11 (Fig. 2) was closed to isolate the cavity from the gas supply. During the cooling, the gas pressure in the pressure vessel was controlled to be 50 Pa to 150 Pa below the pressure within the resonator. Thus, the resonator was under nearly isotropic (hydrostatic) pressure at every temperature.

The two results of the cooling measurements were: (1) the cavity's average coefficient of linear thermal expansion was $\alpha_T = (dL/dT)/L = 1.049\times10^{-5}\ \mathrm{K}^{-1}$ and, (2) the optical length of the axis of the cavity was $L_{\rm opt}(T_{\rm TPW}$, 94.921 kPa) = 129.36470 mm. The fringe counting contributed a standard relative uncertainty of 0.42×10^{-6} to the determination of k_B.

5.1.5 Deformations from bolts, gravity, and pressure

As discussed above, we made a comparatively coarse measurement of the cylinder's length using a coordinate measuring machine before installing the end-plates to conduct two-color interferometry and we used the result of the coordinate measurements in the excess-fraction calculation for the two-color laser interferometry. Each endplate was secured to the cylinder with twenty M8 bolts. Each bolt was tightened with an indicating torque-wrench to a maximum torque of about 4 N·m. While we tightened the bolts, we monitored the length of the 130 mm cylinder with the 633 nm laser in one, fixed position. The interference pattern did not change significantly. We would have detected a change in the length of order 633 nm/2 or an equivalent change in the angle between the endplates. We estimated the deformation of the cylinder generated by the bolts holding the end-plates in position using the ABAQUS/CAE analysis tools. The estimate assumed that the coefficient of friction between the bolts and the threads inside the cylinder was 0.5. Under these conditions, the calculated deformation from the bolts was 0.46 μm which is smaller than the allowable uncertainty (± 0.96 μm) of the coarse measurement. The deformation on the order of 10 nm from gravity contributed a standard relative uncertainty of 0.15×10^{-6} to the determination of k_B.

The cylindrical resonator was installed in a pressure vessel filled with argon.

During the acoustic measurements, the pressure inside the resonator was maintained 50 Pa to 200 Pa higher than the pressure outside the resonator. We used the ABAQUS/CAE analysis tools to calculate the elastic response of the resonator to these small pressure differences. They changed the cavity's length by less than 0.01 μm. Our analysis corrected the resonance frequencies for this effect.

While the acoustic measurements were made, the argon pressures within both the resonator and the pressure vessel were varied in the range 30 kPa to 500 kPa thereby subjecting the resonator to significant hydrostatic pressures. Using the values of Young's modulus and Poisson's ratio mentioned above, we accounted for the effect of hydrostatic pressure on the length of the cavityto obtain $L_{\mathrm{opt}}(T_{\mathrm{TWP}}, p)$ = 129.36473 mm × $[1 - 2\times10^{-6}\,(p/\mathrm{MPa})]$. Because this contraction is a linear function of the pressure, it has no influence on the determination of k_{B}; however, it will slightly affect the value of the second acoustic virial coefficient determined by fitting the corrected resonance frequencies to a polynomial function of the pressure.

5.1.6 Difference between optical length and acoustic length.

The inside surface of each endplate had a partially reflective metallic coating protected by a dielectric overlayer. The manufacturer estimated the thickness of each coating + overlayer was between 5 nm and 20 nm. The laser beams penetrated an unknown distance up to 20 nm into the metallic coating on each end-plate. [23,25] Therefore, we assume the optical length of the cavity was approximately 40 nm longer than the acoustic length. When calculating the speed of sound, we reduced the optical length by the fraction 0.31×10^{-6} and added ½ of this value to the uncertainty of the acoustic length.

$$L = L_{\mathrm{acoustic}} = \left(129.36469\ \mathrm{mm}\right)\times\left[1-2\times10^{-6}\left(p/\mathrm{MPa}\right)\right] \tag{21}$$

The contribution to $u_{\mathrm{r}}(k_{\mathrm{B}})$ is 0.30×10^{-6} from the optical-acoustic difference

5.2 Temperature measurement

The temperature of the argon was measured with three 25 Ω standard capsule-type platinum resistance thermometers (Hart 5686) we embedded in the steel cylinder surrounding the cavity. We calibrated the thermometers in a triple-point-of-water cell that agreed with China's national reference triple-point standard within ±0.03 mK, after the correction for the isotopic abundances in the water.

We observed that humidity interfered with the calibration of the thermometers. To eliminate the humidity effect, we encapsulated the thermometers in 300 mm long, thin-walled, stainless-steel tubes filled with argon. We used a thin layer of thermally conducting grease to improve the thermal contact between the thermometers and the steel capsules. After encapsulating the thermometers, the humidity effect was not detected during repeated calibrations spanning tens of days. During the calibrations, each thermometer was periodically cycled between room temperature and T_{TPW}. The largest change observed during the calibration of the three thermometers was equivalent to 0.13 mK.

After completing the calibrations, the thermometers, HS 195, HS 159 and HS 192, were installed at the upper, middle and the bottom of the cylinder, respectively. We used a thin layer of thermally conducting grease in each well to improve the thermal contact between the thermometer and well. During two months of measurements, the thermometer at the top of the cylinder consistently read 0.1 mK warmer than the thermometer at the bottom. The thermometer in the middle of the cylinder read as much as 0.4 mK warmer than the thermometer at the top. We calculated the temperature of the argon within the resonator from average of the three thermometer readings. During the measurement of a set of acoustic frequencies [modes (200) to (700)] the maximum temperature variation was less than 0.2 mK.

Thermometry contributed to the uncertainty of k_{B} through uncertainties in the calibration and the stability of thermometers, the temperature measurements, and temperature gradients. The maximum temperature change between thermometer calibrations (0.13 mK) was counted as a type B uncertainty with the relative value

$u_r(T) = 0.48\times10^{-6}$. The temperature of gas was assumed to be the average reading of the three thermometers; therefore, half of the maximum gradient (0.4 mK)/2, was assumed to be a type B uncertainty $u_r(T) = 0.73\times10^{-6}$. The gas temperatures varied during the frequency measurements. The maximum variation was 0.2 mK, which was counted as a type B uncertainty $u_r(T) = 0.73\times10^{-6}$.

5.3 Impurity and isotopic composition

We used "BIP" pure argon gas from Air Products for the acoustic measurements. As shown in Fig. 2, the gas flowed from the manufacturer's cylinder through a getter (Aeronex GateKeeper) into the resonator. We collected a sample of the gas after it had passed through the getter and we had the sample analyzed by the Center for Gas Metrology, Korea Institute of Standards and Science (KRISS). The results of the analysis for chemical impurities are listed in Table 2 and the results of the analysis for the relative abundances of the argon isotopes are shown listed in Table 3. We expected the getter would remove the chemically reactive impurities such as hydrocarbons, H_2O, O_2, CO_2, and CO from the working gas; therefore, we were surprised by the comparatively large [(19.0±0.9) μmol/mol] concentration of nitrogen in the gas sample.

Impurities change the zero-pressure limit of the speed of sound c_0; therefore, the uncertainties of the impurity concentrations contribute to the uncertainty of our determination of k_B. Using the methods from [3] and the uncertainties in Table 2, we concluded that the chemical impurity contribution to the relative uncertainty of the zero-pressure speed of sound at T_{TPW} was: $u_r(c_0) = 1.2\times10^{-6}$; this conclusion also appears in Table 7.

The KRISS results in Table 3 determine the value $M_{Ar} = (39.947\,843 \pm 0.000\,028)$ $g\cdot mol^{-1}$ for the molar mass of the commercially-purchased, "BIP" argon that we used for the acoustic measurements. (The relative uncertainty, $u_r(M_{Ar}) = 0.7\times10^{-6}$, appears in Table 7.) Figure 4, compares our KRISS result for M_{Ar} with other measurements for commercially-purchased argon. Our value (labeled “This work”) is close to the average of all of the measurements shown except the anomalous “NPL #1” sample.

The agreement of our KRISS result with the other results in Fig. 4 is evidence against hypothetical, correlated uncertainties among recent determinations measurements of k_B. Recently, Valkiers *et als*. [29] at the Institute for Reference Material and Measurements (IRMM) measured the relative isotopic abundance ratios Ar^{36}/Ar^{40} and Ar^{38}/Ar^{40} in argon from 8 commercial sources and calculated 8 values of M_{Ar} with the remarkably small uncertainty $u_r(M_{Ar}) = 0.09 \times 10^{-6}$. The IRMM results are plotted on Fig. 4 as 8 points between “Lee” and “This work”. The 8 IRMM results include three samples that were recently used to determine provisional values of k_B at National Metrology Institutes, specifically, NPL #1 and NPL #2 [7], and LNE #1 [30], If there were an undetected bias in the IRMM results, it would affect both of these recent determinations of k_B equally. Our result and the three older points on the left of Fig. 4 do not rely on the IRMM data; therefore, they provide a bound on any possible bias. The point on the left labeled “Nier” displays his results [31] for commercial argon obtained by mass spectrometry in 1950. The two values of M_{Ar} on Fig. 4 labeled NIST-M and NIST-A were used to determine k_B at NIST in 1988. [3] These two values of M_{Ar} did not rely on sophisticated mass spectrometry. Instead, the NIST group purchased a sample of isotopically enriched Ar^{40} to use as a mass standard and they used their acoustic resonator to determine the ratio $(M_{Ar,commercial})/(M_{Ar\text{-}40})$.

Figure 4 does not display one value of M_{Ar} obtained from a non-commercial source by Nier [31] and one obtained by Lee *et als*. [32] because these values of M_{Ar} might depend upon the method of purification. We note that the samples INRIM-A and INRIM-B [11] were used in acoustic determinations of thermodynamic temperature ratios. This application requires M_{Ar} to be constant; however, it does not require that M_{Ar} to be accurately known.

5.4 Frequency Measurements

5.4.1 Fitting resonance frequencies f_N and half-widths g_N

We used the procedure described in Ref. [3] to measure the resonance frequencies f_N and the half-widths g_N. After estimating f_N and g_N from either a preliminary measurement or a theoretical model, we stepped the drive transducer through 13 synthesized, discrete frequencies in equal increments starting at $f_N - 2.5g_N$ and ending at $f_N + 2.5g_N$. Then, the frequency sweep was reversed by starting at $f_N + 2.5g_N$ and ending at $f_N - 2.5g_N$. At each frequency, the in-phase voltage u and the quadrature voltage v generated by the detector transducer were measured by a lock-in amplifier. The 26 frequencies and complex voltages were fitted by the resonance function:

$$u + iv = \frac{ifA}{f^2 - (f_N + ig_N)^2} + B + C(f - \tilde{f}) + D(f - \tilde{f})^2 \qquad (22)$$

where, A, B, C and D are complex constants; $F_N = f_N + ig_N$ is the complex resonance frequency of the mode N under study; the parameter $\tilde{f}$ is fixed and is usually taken as the average frequency for the data in the fit. The parameters B and C account for the effects of possible cross talk and the "tails" of the modes other than N. In all the fits, the term $D(f - \tilde{f})^2$ in Eq. (22) was significant.

The contributions to g_N in Eq. (22) from the thermal and viscous boundary layers vary as $f^{-1/2}$. This phenomenon generates a small asymmetry in the shape of the resonance. To account for this, we used the correction

$$\Delta f_N = f_{\text{corrected}} - f_N \approx -f_N \big/ \left(8Q^2\right) \qquad (23)$$

derived by Gillis et als. [33] In this work, the smallest value of the Q was 350 [mode (200) at 50 kPa] where the, the fractional correction to f_N is 1.0×10^{-6} and the fractional correction to k_B is twice as large.

5.4.2 Uncertainty of resonance frequency measurements

The measured resonance frequency f_N is related to the unperturbed (ideal) resonance frequency f_N^0 by

$$f_N^0 = f_N - \Delta f_{\mathrm{b}} - \Delta f_{\mathrm{d}} - \Delta f_{\mathrm{sh}} - \Delta f_{\mathrm{tr}} \tag{24}$$

where $\Delta f_{\mathrm{b}} \equiv (\Delta f_{\mathrm{th}} + \Delta f_{\mathrm{v}})$ is the sum of the thermal and viscous boundary layer perturbations; Δf_{d} is the perturbation from a fill duct; $\Delta f_{\mathrm{sh}} \equiv \Delta f_{\mathrm{sh1}} + \Delta f_{\mathrm{sh2}} + \Delta f_{\mathrm{sh3}} + \Delta f_{\mathrm{sh4}}$ is the sum of the perturbations from the shell's motion, and Δf_{tr} is the perturbation from the transducers..

In Ref. [34], one of us estimated the relative uncertainties of the viscosity $u_{\mathrm{r}}(\eta_{\mathrm{Ar}}) \approx 0.00025$ and the thermal conductivity $u_{\mathrm{r}}(\lambda_{\mathrm{Ar}}) \approx 0.00025$ of argon in the limit of zero density at 273.16 K. Using these estimates in Eqs. (4) and (8) leads to an estimated relative uncertainty of the thermo-acoustic boundary layer correction: $u_{\mathrm{r}}(\Delta f_{\mathrm{b}}) \approx 0.00013$. For the worst case $l = 2$ and $p = 50$ kPa, $\Delta f_{\mathrm{b}} / f_2^0 \approx \Delta f_{\mathrm{b}} / f_2 \approx -0.0016$ and its contribution to $u_{\mathrm{r}}(k_{\mathrm{B}})$ is $2u(\Delta f_{\mathrm{b}})/f_N \approx 0.4\times10^{-6}$. This uncertainty is negligible in comparison with other, larger contributions to the uncertainty budget.

The imprecision of a measurement of f_N and g_N is proportional to $g_N/(s/n)$, where s/n denotes the signal-to-noise ratio of a measurement of the acoustic pressure. The drive transducer generates an acoustic pressure $k{\cdot}p{\cdot}Q$, where p is ambient pressure, $Q \equiv f_N/(2g_N)$ is the quality factor, and k is a dimensionless proportionality factor for our apparatus. The acoustic detector generates the signal $s = k'{\cdot}k{\cdot}p{\cdot}Q$. For our cavity at the lower pressures, $1/(2Q) = g_N/f_N \approx 0.6\,(p/\mathrm{kPa}{\cdot}f/\mathrm{Hz})^{-1/2}$. Therefore, at low pressures, the random error of resonance frequency measurements varies as $\delta f_N / f_N \approx \left(g_N / f_N\right)\left[n/\left(k'kpQ\right)\right]$. For the high Q resonances at high pressures, we observed that $\delta f_N/f_N \approx 2\times10^{-7}$. Thus, the random noise in our measurement was approximated by the function

$$\frac{\delta f_N}{f_N} \approx 2\times10^{-7} + 24\left(\frac{\mathrm{Hz}}{f}\right)\left(\frac{\mathrm{kPa}}{p}\right)^2 \quad . \tag{25}$$

The loss of precision in the data below 100 kPa was obvious.

5.4.3 Frequency measurements at T_{TPW}

To prepare for the measurements, the resonator assembly, the rotation stage, and the pressure vessel were installed in the thermostat at room temperature. The resonator, the pressure vessel, and the gas manifold were purged automatically with the working argon gas for more than 48 hours. During this purging process, the entire system was baked at 55 °C, except for the differential pressure gauge (Baratron 616A) which was baked at 120 °C. During each frequency measurement, the valve leading from the fill duct to the gas manifold was closed.

During each of three successive runs, we measured the resonant frequencies of the modes (200) through (700) as the pressure was decreased in steps from 500 kPa to 50 kPa. The results from the three runs were mutually consistent. During the 4-hour-long interval required to measure f_2, …, f_7, the cylinder's steady-state temperature was within 2 mK of T_{TPW} and it was stable to 0.1 mK.

When the frequency measurements on each pressure step were completed, the valves leading to the gas-handling system were opened and the pressures inside the resonator and the pressure vessel were reduced to the next pressure and maintained constant. As the pressure decreased, the adiabatic expansion of the argon cooled the cylinder. We returned the cylinder to T_{TPW} using a heater glued on the outside of the cylinder near its center.

Between each of the 3 runs, the cylindrical cavity was repeatedly evacuated and filled with the argon working gas for at least 12 hours. While this purging proceeded, the gas manifold was baked. Once the purging was completed, the cavity was filled with argon to 500 kPa to begin the next run.

We were unable to acquire useful data for the modes (800) and (900) because these modes partially overlapped other modes of the gas-filled cavity and/or the shell surrounding the cavity.

5.5 Analysis of speed-of-sound measurements

The speeds of sound were computed from the corrected frequency measurements and the cavity's lengths at the experimental temperatures and pressures T and p. Then, the speeds of sound were computed exactly at T_{TPW} using the relation

$$c^2\left(T_{\mathrm{TPW}}, p\right) = \left(T_{\mathrm{TPW}} / T\right) c^2\left(T, p\right) \quad . \tag{26}$$

The acoustic model for the cylindrical resonator does not include terms on the order $(\delta_v/a)^2$ and $[(\gamma - 1)(\delta_T/a)]^2$. The approximate values of these terms are $(\delta_v/a)^2 \approx 2.0\times10^{-6}\times(100\text{ kPa})/(l\cdot p)$ and $[(\gamma - 1)(\delta_T/a)]^2 \approx 1.3\times10^{-6}\times(100\text{ kPa})/(l\cdot p)$ in the range of our measurements (modes l = 2 to 7; $T = T_{\mathrm{TPW}}$; 30 kPa < p < 550 kPa) Thus, neglecting these unknown terms might produce an l-dependent trend in the values of c_0^2 determined for the various modes. Because of this concern, we did not take data for the l =1 mode. (Also, the corrections to f_{100} from the fill duct are very large and uncertain.) As the pressure decreases, the neglected terms increase as p^{-1} and the signal-to-noise ratio of the frequency measurements decreases as p^2. (See Section 5.4.2.) Therefore, we reduced the weight of the data below 100 kPa as $(p/100\text{ kPa})^2$.

Figure 5 provides a compact overview of our results. We plot the scaled differences $10^6(c^2 - c_{\mathrm{ref}}^2)/c^2$ between our measurements of c^2 using 6 modes and "reference" values of c^2 reported in Ref. [3]. This comparison does not require fitting various functions to our data. The differences $10^6(c^2 - c_{\mathrm{ref}}^2)/c^2$ are nearly linear functions of the pressure for each mode. The differences tend to decrease as the pressure decreases; however, they do not vanish at zero pressure. We quantified this comparison by fitting the equation

$$c_l^2\left(T_{\mathrm{TPW}}, p\right) - c_{\mathrm{Ref}}^2\left(T_{\mathrm{TPW}}, p\right) = \Delta A_{0,l} + \Delta A_{1,l}\, p \quad . \tag{27}$$

to our data between 100 kPa and 550 kPa for each mode separately. The unweighted average of the intercepts $\Delta A_{0,l}$ for the 6 modes gave $\left\langle c_0^2 \right\rangle$ = 94756.47 m^2 s^{-2} with a standard deviation of 7.2 ppm. This average intercept is 3.1 ppm higher than the reference value 94756.178 m^2 s^{-2} [3]. Because the inconsistencies among the modes at zero pressure exceed the noise, we expect that improved construction and/or modeling will reduce the uncertainty of c_0.

In order determine the speed-of-sound of the ideal gas c_0 without referring to Ref. [3], we simultaneously fit the 130 measured frequencies $f_{l,i}$ over the entire pressure range with the system of equations with 14 adjustable parameters

$$\left[\left(\frac{2L_i}{l}\right)\left(f_{l,i}+\Delta f_{l,i}\right)\right]^2 - A_3 p_i^3 = A_{0,l} + A_{1,l} p_i + A_2 p_i^2 + A_{-1} p_i^{-1} . \qquad (28)$$

Here, the six modes are denoted by $l = 2\ldots7$, and n_l is the number of data points for mode l. ($n_l = 22$ for $l = 3,4,6,7$, and $n_l = 21$ for $l = 2$ and 5.) The length of the cavity L_i is subscripted because it depends on the pressure and temperature of the ith point. Six of the adjusted parameters were the intercepts $A_{0,l} \equiv c_{0,l}^2$ for each mode and six parameters were the slopes $A_{1,l}$ for each mode. These coefficients are mode-dependent because of the imperfections in our models for the compliance of the shell and the shape of the cavity, as discussed in Section 2.2. The parameter $A_2 \equiv 5\gamma_\mathrm{a} / (3M_\mathrm{Ar})$ is a multiple of the third acoustic virial coefficient γ_a; therefore, we assumed that it had the same value for every mode. Because c_0 is only weakly sensitive to A_3 we fixed A_3 at the value 1.45×10^{-18} m^2·s^{-2}·Pa^{-2} taken from Ref. [35]. The parameter A_{-1} accounts for the thermal and momentum accommodation coefficients and we also assumed that it had the same value for every mode.

The minimization function χ^2 was a weighted sum of the squared deviations from Eq. (28). The deviation at each frequency and pressure was weighted by the quantity $w(f_i, p_i) = \left[\sigma(f_i, p_i)\right]^{-1}$, where $\sigma(f, p) = 2c^2 \left|\Delta f_N / f_N\right|$ and $\left|\Delta f_N / f_N\right|$ was obtained from Eq. (25). The results of the surface fit are listed Table 4 in the column designated "fit 1" and the scaled deviations for the fit are displayed in Fig. 6. The uncertainties given in Table 4 reflect the statistical uncertainties for the coefficients from the fit. The uncertainty for coefficient A_α was calculated using $\sqrt{\varepsilon_{\alpha\alpha}\chi^2 / N_\mathrm{df}}$, where $\varepsilon_{\alpha\alpha}$ is the diagonal element of the covariance matrix and N_df is the number of degrees of freedom in the fit. The average of the coefficients

$\left\langle A_{0,l} \right\rangle = c_0^2$ for the 6 modes is 94756.36 $m^2 \cdot s^{-2}$ with a standard deviation of 0.72 $m^2 \cdot s^{-2}$ and a relative uncertainty $u(c_0^2)/c_0^2$ of 7.6 ppm. The average of the coefficients $\left\langle A_{1,l} \right\rangle = A_1$ is $2.227 \times 10^{-4}\ \mathrm{m^2 \cdot s^{-2} \cdot Pa^{-1}}$ with a standard deviation of $0.061 \times 10^{-4}\ \mathrm{m^2 \cdot s^{-2} \cdot Pa^{-1}}$. This value of A_1 is equivalent to the value $\beta_\mathrm{a} = \left(5.34 \pm 0.15\right) \times 10^{-6}\ \mathrm{m^3 \cdot mol^{-1}}$ for second acoustic virial coefficient.

The result χ^2 =186 for 116 degrees of freedom and also the observation (Fig. 6) that 9 scaled deviations fall outside the range ±2 σ suggest that our *a priori* estimate of the frequency uncertainties was 30 % too small; however, it is satisfying that the scaled deviations do not have obvious pressure- or mode- dependences.

Fit 1 yielded the value A_{-1} = (4.1 ± 7.3)×10^3 $m^2 \cdot s^{-2} \cdot Pa$, which indicates that its value could not be determined from these data. To demonstrate that $A_{-1} \equiv 0$ is consistent with the data, we refit the data with A_{-1} fixed at 0. The results are in Table 4 in the column labeled “fit 2”. Fixing $A_{-1} \equiv 0$ did not change χ^2 significantly, and it increased the average $A_{0,l}$, by 0.62 ppm. We treat this as an added uncertainty in the determination of k_B. The results from from the mode fits and the surface fits are summarized in Table 5.

As mentioned above, the differences between values of c_0^2 determined from the 6 longitudinal modes are larger than their respective uncertainties. We suspect that our incomplete understanding of some imperfections in the cavity’s shape contribute to these mode inconsistencies. The imperfection associated with the fill duct produces a large perturbation with a large uncertainty that affects the even longitudinal modes, but not the odd modes. The value of k_B determined when we excluded the even modes from the analysis was, fractionally, (5.0 ± 5.2)×10^{-6} smaller than the CODATA value.

5.6 Determination of k_B

The Boltzmann constant k_B was re-determined by Eq. (3) based on the speed-of-sound of idea gas c_0, the triple point of water T_{TPW}, the molecular mass M, the Avogadro constant N_A, and the ratio of specific heat capacity for ideal gas γ_0. The new determination of k_B is $1.380\,650\,6\times10^{-23}\ \mathrm{J\cdot K^{-1}}$, which is 0.12×10^{-6} above the value recommended in CODATA 2006. Table 6 compares our new determination of k_B and other acoustic determinations of k_B with the value recommended by CODATA in 2006. [18] All of the tabulated values agree, within combined uncertainties, with the CODATA recommendation and none claim smaller uncertainties than the CODATA value.

6 Uncertainty budget

The Boltzmann constant k_B is connected to measured quantities (frequencies f_l, mode l, length L, temperature T, pressure p), calculated frequency perturbations Δf_l, the fundamental constant N_A, quantities measured by others (A_3, M_{Ar}), and fitted quantities ($A_{1,l}$, A_2, A_{-1}) through the relation

$$k_B = \frac{3M_{Ar}}{5TN_A}\left[\left(\frac{2L}{l}\right)^2 (f_l+\Delta f_l) - A_{1,l}p - A_2p^2 - A_3p^3 - \frac{A_{-1}}{p}\right] \quad . \tag{29}$$

Thus, the relative uncertainties $u_r(M_{Ar})$ $u_r(T)$, and $u_r(L^2)$ contribute directly into the relative uncertainty of $u_r(k_B)$. [For $u_r(L^2)$, this is an excellent approximation because the L^2 term in the square brackets of Eq. (29) is at least 800 times larger than the other terms.] The uncertainties of calculated perturbations $u(\Delta f_l)$ contribute to $u_r(k_B)$ in a complicated way that we explored by numerical experiments. Table 7 lists all our estimates of contributions to $u_r(k_B)$ from these known sources and includes references to the appropriate sections of this manuscript for the estimates.

As discussed in Section 5.5, each of the 6 modes $2\leq l \leq 7$ were fit by Eq. (29) independently and yielded independent values of k_B. The resulting values of k_B differed from each other by more than their estimated uncertainties. We treated the standard deviation of these values from their mean as an additional contribution to the uncertainty of k_B and we refer to it as "inconsistency among modes". These inconsistencies are anomalous because we do not know their source. They are a quantitative measure of the how our real resonator differs from our model for the resonator.

Figure 7 provides a completely independent, quantitative measure of how our real resonator differs from our model for the resonator. Figure 7 is a plot of the difference between the measured and calculated half-widths of the resonances $\Delta g \equiv (g_{\mathrm{meas}} - g_{\mathrm{calc}})$. When Δg is multiplied by $2\times10^{-6}/f$ and plotted, it is analogous to the speed-of-sound difference $10^6(c^2 - c_{\mathrm{ref}}^2)/c^2$ plotted in Fig. 5, insofar as both quantities are computed from the data and model without fitting any parameters. Because g_l and f_l are the real and imaginary parts of a single complex frequency, it is reassuring that the values of $2\times10^{-6}\Delta g/f$ are comparable to the values $10^6(c^2 - c_{\mathrm{ref}}^2)/c^2$. However, the consistently negative values of Δg for the $l = 4$ mode are anomalous. (A truly negative Δg would violate conservation of energy.) At the end of the following section, we speculate about the origins and cures of the anomalous inconsistency among the modes and on the anomalous negative values of Δg.

7. Summary and discussion

We used a single acoustic cylindrical resonator to re-determine k_{B}. Our result, $k_{\mathrm{B}} = 1.380\,650\,6\times10^{-23}\ \mathrm{J\cdot K^{-1}}$ has the relative standard uncertainty: $u_{\mathrm{r}}(k_{\mathrm{B}}) = 7.6\times10^{-6}$ and is, fractionally, 0.12×10^{-6} above the value determined by CODATA in 2006 [18]. Our result agrees, within combined uncertainties with other determinations of k_{B} that used spherical and quasi-spherical resonators [3,5,6,7]. We also determined the second acoustic virial coefficient $\beta_{\mathrm{a}} = 5.34 \pm 0.15\ \mathrm{cm^3\cdot mol^{-1}}$. This result agrees, within combined uncertainties, with the values of β_{a} clustered about 5.4 $\mathrm{cm^3\cdot mol^{-1}}$ that were determined using spherical and quasi-spherical resonators. [3,7,12,20,21,22] This value of β_{a} does not agree with the value $\beta_{\mathrm{a}} = (4.92\pm0.34)\ \mathrm{cm^3\cdot mol^{-1}}$ previously determined using a highly-accurate, variable-length cylindrical resonator. [2] Finally, we determined the quadratic term in Eq. (29): $A_2 = (5.188 \pm 0.051)\times10^{-11}\ \mathrm{m^2\cdot s^{-2}\cdot Pa^{-2}}$.

Our value for A_2 does not agree, within combined uncertainties, with the value $A_2 = (5.321 \pm 0.062)\times10^{-11}\ \mathrm{m^2{\cdot}s^{-2}{\cdot}Pa^{-2}}$ reported in Ref. [3]. These results for k_B and β_a suggest that many aspects of our resonator are well understood. Nevertheless, the anomalous inconsistencies of c^2 as $p\rightarrow0$ in Fig. 5 and the anomalous negative values of Δg in Fig. 7 show that our understanding of the cylindrical resonator is incomplete.

We speculate that the both anomalies may have resulted, in part, from our use of an inadequate protocol for determining resonance frequencies. As described in Section 5.4.1, we determined the complex resonance frequencies by fitting voltage-*vs*-frequency data with Eq. (22) to determine the values of f_N and g_N. Then, we used Eq. (23) to correct f_N and g_N for the asymmetry in the shape of low-Q resonances. However, Eq. (23) is a numerical approximation that was determined in [33] for the particular frequency span $f_N \pm 2g$ and a particular combination of acoustic surface losses and bulk viscosity. In the future, we shall fit the voltage-*vs*-frequency data to a more exact version of Eq. (22) where the constant g_N is replaced with the frequency-dependent function that is appropriate for our mode- and pressure-dependent combination of frequency span, surface, bulk-viscosity, and duct losses.

We noticed that the unperturbed $l = 4$ mode at 4.76 kHz has two near neighbors, the (001) mode at 4.69 kHz and the (101) mode at 4.84 kHz. Also, the $l = 5$ and $l = 7$ modes each have one near neighbor. To deal with closely spaced neighbors, we will enlarge the span of the voltage-*vs*-frequency data to include the neighboring modes and find the values of F_N that best fit the neighboring modes.

Minor changes of the present apparatus should improve the results. In the future we will use a fill duct with a smaller inside diameter, and we will fill the gap where the duct joins the cavity. This will reduce the perturbations and their uncertainties. We expect that some or most of the anomalies will be reduced.

More complicated improvements are possible. In [9], we proposed an innovative two-resonator method for determining k_B. Both cylindrical resonators will have the same diameter cavity and their lengths will be in the ratio 2:1. We will exploit the 2:1 length ratio to study several longitudinal resonances in both resonators at the same frequency and we will transfer a pair of end-plates from one resonator to the other. Furthermore, the fill duct will enter the resonator through the endplate. The frequency-dependent corrections from the end-plates, including those from the fill duct will be nearly identical in both resonators; therefore, they can be eliminated by combining the measurements from the two resonators. Similarly, the optical effects of the semi-transparent metal films can be eliminated from the combined measurements. Thus, we expect the two-cylinder method will significantly reduce $u_r(k_B)$.

Finally, we are conducting experiments to establish the feasibility of using non-degenerate TM microwave resonances to determining the dimensions of a fixed-length, cylindrical cavity. [17] Microwave length measurements are likely to be simpler than optical length measurements, particularly when working at very high or very low temperatures where optical access is difficult. The combination of microwave resonances and acoustic measurements in the same cavity can be used to accurately determine the dielectric properties of gases and solids.

Acknowledgments The authors thank D.C. Ripple of NIST and F. Pavese of INRiM for their helpful suggestions to prevent gas contamination. We thank James B. Mehl for his valuable analyses of the shell motions of cylinder cavity. We thank L. Pitre, R. Gavioso, and M. de Podesta for their kind concerns and encouragement. We are grateful to Ms Deullae Min and Dr. Jin Seog Kim of KRISS for their timely analysis of our argon sample. This work was supported by the National Science and Technology Pillar Program (2006BAF06B00) and the National Natural Science Foundation of China (No. 50906076 and No. 51076074).

Table 1. Perturbations for fixed path cylinder resonator

Quantity	Unit	Relationship
Measurement frequency correction	Hz	$f_{\text{corrected}} - f_N = -f_N / \left(8Q^2\right)$ and $g_{\text{corrected}} - g_N = -g_N / \left(4Q^2\right)$
2nd viral coefficient [20]	$\text{m}^3 \cdot \text{mol}^{-1}$	$B(T) = \left(34.1954 - 1.1599 \times 10^4 T^{-1} - 9.62070 \times 10^5 T^{-2}\right) \times 10^{-6}$
Second acoustic virial coefficient	$\text{m}^3 \cdot \text{mol}^{-1}$	$\beta_{\text{a}}(T) = 2B + 2(\gamma_0 - 1)\frac{\text{d}B}{\text{d}T} + \frac{(\gamma_0 - 1)^2}{\gamma_0}\frac{\text{d}^2 B}{\text{d}T^2}$
Density	$\text{mol} \cdot \text{m}^{-3}$	$\rho(p, T) \approx \frac{p}{RT}\left(1 - B\frac{p}{RT}\right)$
Constant pressure heat capacity	$\text{J} \cdot \text{kg}^{-1} \cdot \text{K}^{-1}$	$C_p(p, T) = \left(\frac{5}{2} - T^2 \frac{\text{d}^2 B}{\text{d}T^2}\frac{p}{RT}\right)\frac{R}{M}$
Ratio of specific heat capacities		$\gamma(p, T) = \frac{5}{3}\left[1 + 2(\gamma_0 - 1) T \frac{dB}{dT}\frac{p}{RT} + (\gamma_0 - 1)^2 T^2 \frac{d^2 B}{dT^2}\frac{p}{RT}\right]$

Thermal conductivity [21,22]	$\mathrm{W\cdot m^{-1}\cdot K^{-1}}$	$\lambda(p,T)=\left[16.3815+0.052\times(T\text{-}273.16)+0.0216\rho\right]\times10^{-3}$
Viscosity [21,22]	$\mathrm{Pa\cdot s}$	$\eta(p,T)=\left[20.9627+0.066\times(T\text{-}273.16)+0.01111\rho(p,T)\right]\times10^{-6}$
Thermal penetration length	m	$\delta_{\mathrm{th}}(p,T)=\sqrt{\dfrac{2D_{\mathrm{th}}}{\omega}}=\sqrt{\dfrac{1}{\pi f}\dfrac{\lambda}{\rho C_P}}$
Viscous penetration length	m	$\delta_{\mathrm{v}}(p,T)=\sqrt{\dfrac{2D_{\mathrm{v}}}{\omega}}=\sqrt{\dfrac{1}{\pi f}\dfrac{\eta}{\rho}}$
Thermal accommodation length	m	$l_{\mathrm{th}}(p,T)=\dfrac{\lambda}{p}\sqrt{\dfrac{\pi MT}{2R}}\dfrac{2-h_{\mathrm{th}}}{h_{\mathrm{th}}}\dfrac{1}{C_{V,m}/R+0.5}$
Viscous accommodation length	m	$l_{\mathrm{v}}(p,T)=\dfrac{\eta}{p}\sqrt{\dfrac{\pi RT}{2M}}\dfrac{2-h_{\mathrm{v}}}{h_{\mathrm{v}}}$

Thermal boundary layer correction	$\frac{(\Delta f_l)_{\text{th}}}{f_l^0} = -\frac{\gamma - 1}{2a}\left[(\delta_{\text{th}} - 2l_{\text{th}})\left(1 + \frac{2a}{L}\right) - \frac{\lambda}{\lambda_{\text{shell}}}\delta_{\text{th,shell}} - \frac{2a}{L}\frac{\lambda}{\lambda_{\text{endplate}}}\delta_{\text{th,endplate}}\right]$
Viscous boundary layer correction	$\frac{(\Delta f_l)_{\text{v}}}{f_l^0} = -\frac{1}{2R}(\delta_{\text{v}} - 2l_{\text{v}})$
*i*th correction for shell motion	$\frac{(\Delta f_l)_{\text{sh},i}}{f_l^0} \approx -\left(\rho c^2\right)_{\text{gas}} \frac{G_{i,l}^* \times 10^{-12} / (\text{m}^3\ \text{J}^{-1})}{1 - \left(f_l^0 / f_{\text{sh}i}\right)^2}$
correction for longitudinal recoil	$\frac{(\Delta f_l)_{\text{sh4}}}{f_l^0} = -\frac{1}{2}\frac{KE_{\text{solid}}}{KE_{\text{fluid}}} = -\left(\frac{2}{l\pi}\right)^2 \frac{M_{\text{gas}}}{M_{\text{res}}}, \text{odd } l$
transducer correction	$\frac{\Delta f_{\text{tr}}}{f_l^0} = -\frac{1}{16}\frac{\left(\rho c^2\right)_{\text{g}}}{\left(\rho_{\text{FS}} c_{p,\text{FS}}^2\right)}\left(\frac{2a}{L}\right)\left(\frac{a_{\text{dm}}}{a}\right)^3\left(\frac{a_{\text{dm}}}{t_{\text{dm}}}\right)^3 \frac{1}{1 - \left(f_l^0 / f_{\text{dm}}\right)^2}$
duct correction [15]	$\frac{\Delta f_{\text{d}}}{f_l^0} = \begin{cases} \text{Re}\left(\frac{iy_{\text{d}} A_{\text{d}}}{l\pi^2 a^2}\right), & l = \text{even number} \\ 0, & l = \text{odd number} \end{cases}$

Contribution of the thermal boundary layer to resonance half-width[23, 13]	$\frac{(g_l)_{\text{th}}}{f_l^0}=\frac{\gamma-1}{2a}\left[\delta_{\text{th}}\left(1+\frac{2a}{L}\right)-\frac{\lambda}{\lambda_{\text{shell}}}\delta_{\text{th,shell}}-\frac{2a}{L}\frac{\lambda}{\lambda_{\text{endplate}}}\delta_{\text{th,endplate}}\right]$
Contribution of the viscous boundary layer to resonance half-width[23, 13]	$\frac{(g_l)_{\text{v}}}{f_l^0}=\frac{\delta_{\text{v}}}{2a}$
Contribution of bulk attenuation of sound to resonance half-width [24, 3]	$\frac{g_{\text{bulk}}}{f_l^0}=\left(\frac{\pi f}{c}\right)^2\left\{\frac{4}{3}\delta_{\text{v}}^2+(\gamma-1)\delta_{\text{th}}^2\right\}$
Contribution of Duct Correction to resonance half-width [14]	$\frac{(g_l)_{\text{d}}}{f_l^0}=\begin{cases}\text{Im}\left(\frac{iy_{\text{d}}A_{\text{d}}}{l\pi^2a^2}\right), & l=\text{even number}\\ 0, & l=\text{odd number}\end{cases}$

Table 2. Impurity analysis of working gas

Component	***Molar mass ($g \cdot mol^{-1}$)**	**Molar mass uncertainty** ($g \cdot mol^{-1}$)**	**Mole fraction (μmol/mol)**	**Fraction uncertainty** (μmol/mol)**
Hydrogen	2.015 88	0.000 07	2.6	0.5
Helium	4.002 602	0.000 001	1.6	0.3
Carbon Dioxide	44.009 5	0.000 5	1.3	3.8
Methane	16.042 46	0.000 43	0.5	0.3
Oxygen	31.998 8	0.000 3	1.6	0.3
Nitrogen	28.013 4	0.000 2	19.0	0.9
Neon	20.179 7	0.000 3	1.1	0.6
Krypton	83.798	0.001	0.3	0.2
Xenon	131.293	0.003	0.5	0.3
Argon	39.947 843	0.000 028	999971.5	4.0

* From Ref. [36]

** Standard uncertainty (1σ).

Table 3. Argon isotopic analysis

Isotope	Fraction of argon	Fraction uncertainty*	**Molar mass ($g \cdot mol^{-1}$)	Molar mass uncertainty* ($g \cdot mol^{-1}$)	Molar mass of argon in sample ($g \cdot mol^{-1}$)
^{36}Ar	0.003 325	0.000 003	35.967 546 26	0.000 000 14	39.947 843 ± 0.000 028
^{38}Ar	0.000 629	0.000 012	37.962 732 2	0.000 000 3	
^{40}Ar	0.996 046	0.000 012	39.962 383 124	0.000 000 003	

* Standard uncertainty (1σ)

**.From Ref. [37].

Table 4. Results of fits to speed-of-sound surface fit at the triple point of water

parameter	fit 1	fit 2
$A_{0,2}$/ m^2 s^{-2}	94757.513 ± 0.12	94757.567 ± 0.075
$A_{0,3}$/ m^2 s^{-2}	94756.428 ± 0.12	94756.482 ± 0.064
$A_{0,4}$/ m^2 s^{-2}	94756.481 ± 0.11	94756.536 ± 0.059
$A_{0,5}$/ m^2 s^{-2}	94755.512 ± 0.11	94755.567 ± 0.057
$A_{0,6}$/ m^2 s^{-2}	94756.600 ± 0.11	94756.655 ± 0.053
$A_{0,7}$/ m^2 s^{-2}	94755.653 ± 0.11	94755.708 ± 0.051
10^4 $A_{1,2}$/ m^2 s^{-2} Pa^{-1}	2.2162 ± 0.0046	2.2142 ± 0.0029
10^4 $A_{1,3}$/ m^2 s^{-2} Pa^{-1}	2.3439 ± 0.0045	2.3419 ± 0.0028
10^4 $A_{1,4}$/ m^2 s^{-2} Pa^{-1}	2.1921 ± 0.0045	2.1901 ± 0.0027
10^4 $A_{1,5}$/ m^2 s^{-2} Pa^{-1}	2.2396 ± 0.0045	2.2377 ± 0.0027
10^4 $A_{1,6}$/ m^2 s^{-2} Pa^{-1}	2.1773 ± 0.0044	2.1753 ± 0.0026
10^4 $A_{1,7}$/ m^2 s^{-2} Pa^{-1}	2.1949 ± 0.0044	2.1929 ± 0.0026
$10^{11}A_2$/ m^2 s^{-2} Pa^{-2}	5.188 ± 0.051	5.209 ± 0.034
$10^{-3}A_{-1}$/ m^2 s^{-2} Pa	4.1 ± 7.3	0
χ^2	186	186

Table 5. Speed of sound mode and surface fits

Parameter	Value (mode fits)	Value (surface fits)
$A_0 / \mathrm{m}^2 \cdot \mathrm{s}^{-2}$	94756.47 ± 0.72	94756.36 ± 0.72
$10^4\ A_1 / \mathrm{m}^2 \cdot \mathrm{s}^{-2} \cdot \mathrm{Pa}^{-1}$	2.219 ± 0.061	2.227 ± 0.061
$10^{11}\ A_2 / \mathrm{m}^2 \cdot \mathrm{s}^{-2} \cdot \mathrm{Pa}^{-2}$	–	5.188 ± 0.051
$\beta_\mathrm{a} / \mathrm{cm}^3 \cdot \mathrm{mol}^{-1}$	5.319 ± 0.15	5.339 ± 0.15
$(M/\gamma_0) / \mathrm{g} \cdot \mathrm{mol}^{-1}$	23.968644 ± 0.000033	

Table 6. Acoustic determinations of k_B compared with the CODATA 2006 value $1.3806504(24)\times10^{-23}$ J·K^{-1} reported in [17].

Source	$\frac{k_B - k_{2006}}{k_{2006}}\times10^6$	Uncertainty $(1\sigma)\times10^6$
This work	0.12	7.6
CODATA 2006 [17]	0.00	1.7
Moldover, et. al. [3]	–0.18	1.7
Sutton, et. al.[11]	–0.58	3.1
Pitre, et. al.[10]	−1.88	$^{+2.34}_{-1.35}$
Gavioso, et. al. [9]	−7.50	7.5
Colclough et. al. [2]	4.0[a]	8.4

[a]Re-calculated using the Avogadro constant from [17]

Table 7. Relative uncertainties for determining k_B.

Uncertainty source	Reference	$10^6\times$(Relative uncertainty)
1. Gas temperature measurement	Sec. 5.2	
Thermometer calibration		0.48
Temperature gradient		0.73
Temperature fluctuation		0.73
2. Avogadro constant,	[18]	0.05
3. Molar mass	Sec. 5.3	
Abundance of impurities		1.2
Isotopic abundance ratios		0.7
4. Length measurement	Sec. 5.1	
Two color interferometry at 20.000 °C		0.46
Optical-acoustic difference		0.30
Length contraction		0.42
Cylinder deformation from gravity		0.15
5. Zero-pressure limit of corrected frequencies	Sec. 5.4	
Boundary layer corrections		0.40
Random error in frequency measurements		0.26
Difference between "fit 1" and "fit 2"		0.62
Root sum of squares known uncertainties		2.1
Inconsistency among six modes		7.6

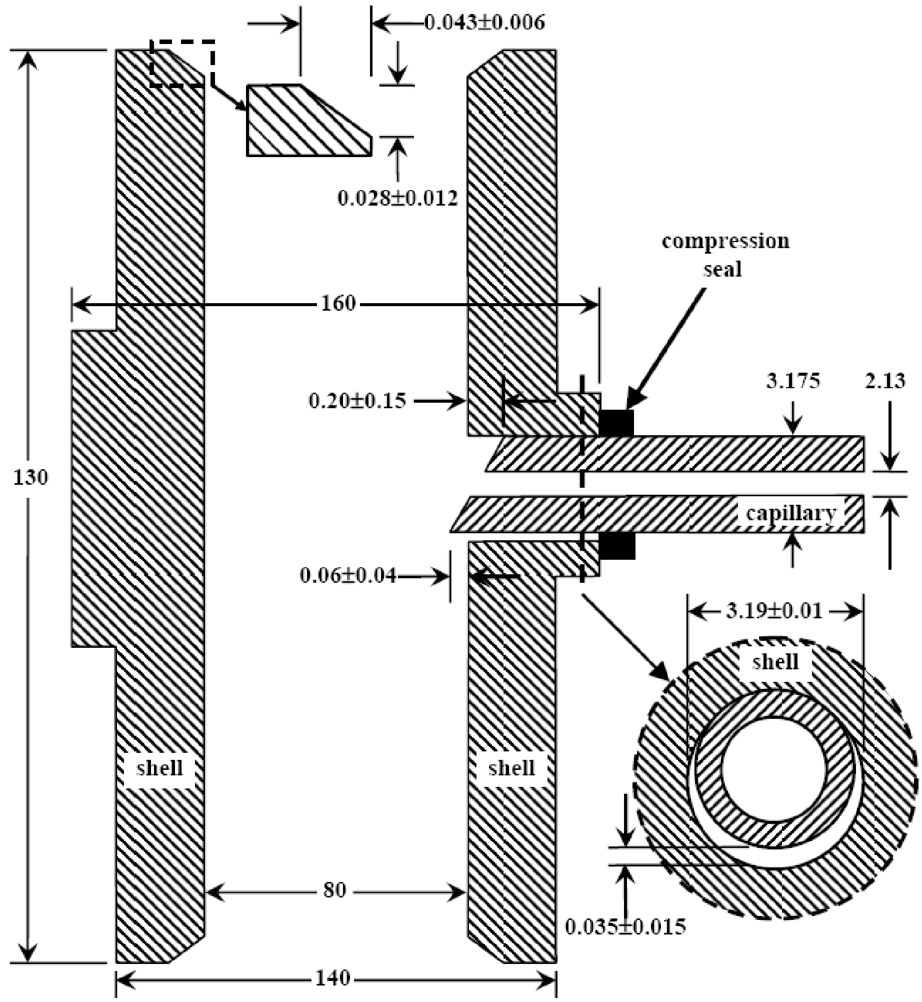

Fig. 1. Diagram of the joint between duct and cylindrical shell. (Not to scale.) All dimensions are in millimeters. Inset in lower right is a model cross-section. The chamfers at the ends of the shell are also noted.

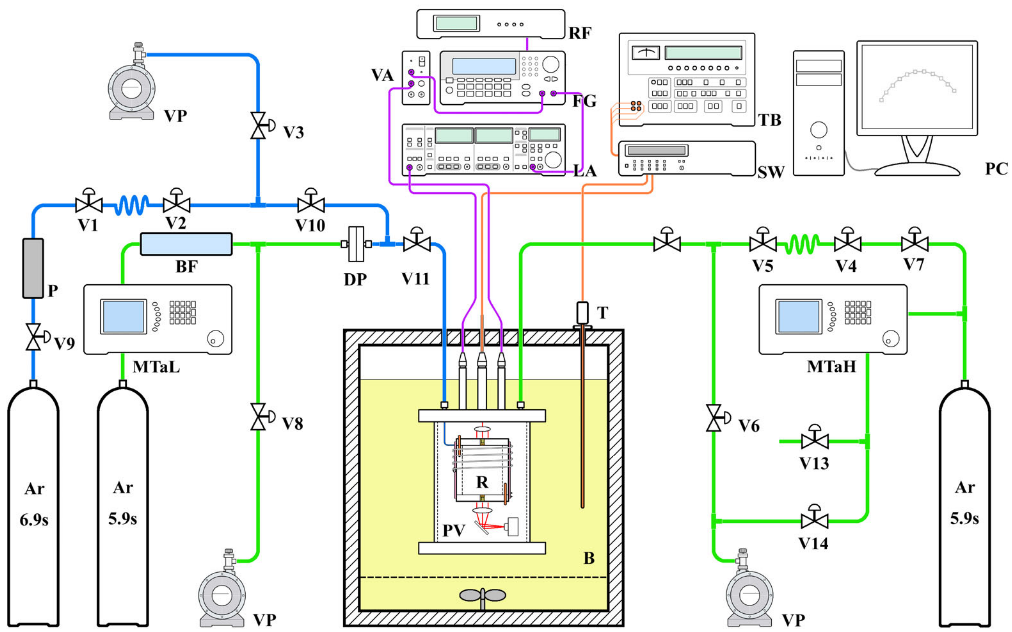

Fig. 2. Sketch of the experimental setup. The labels refer to: B, thermostat bath; BF, buffer volume; DP, differential pressure transducer; FG, functional generator; LA, lock-in amplifier; MTaH/L, absolute manometer; P, purifier; PC, computer; PV, pressure vessel; R, resonator; RF, GPS reference frequency; SW, selector switch; T, thermometer; TB, thermometer bridge; VP, vacuum pump; V1-V14,

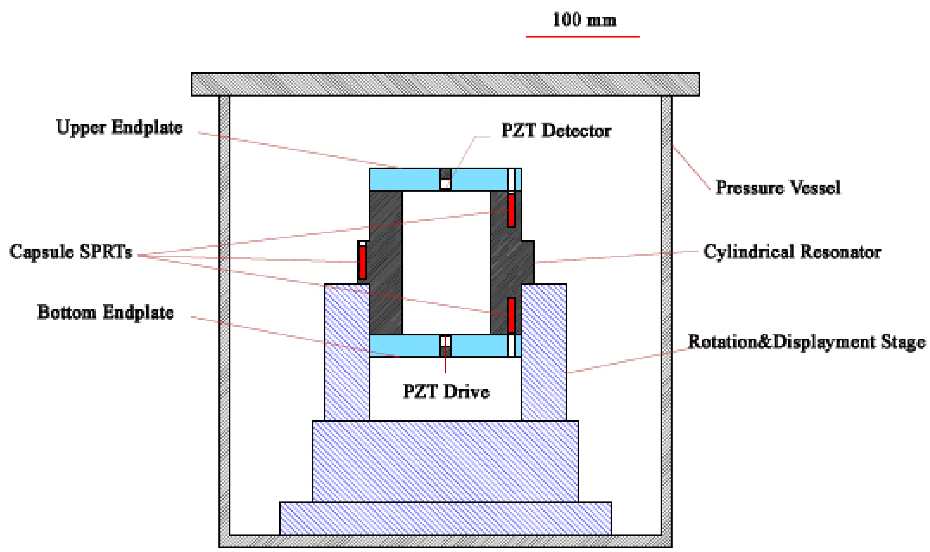

Fig. 3. Cylindrical resonator assembly

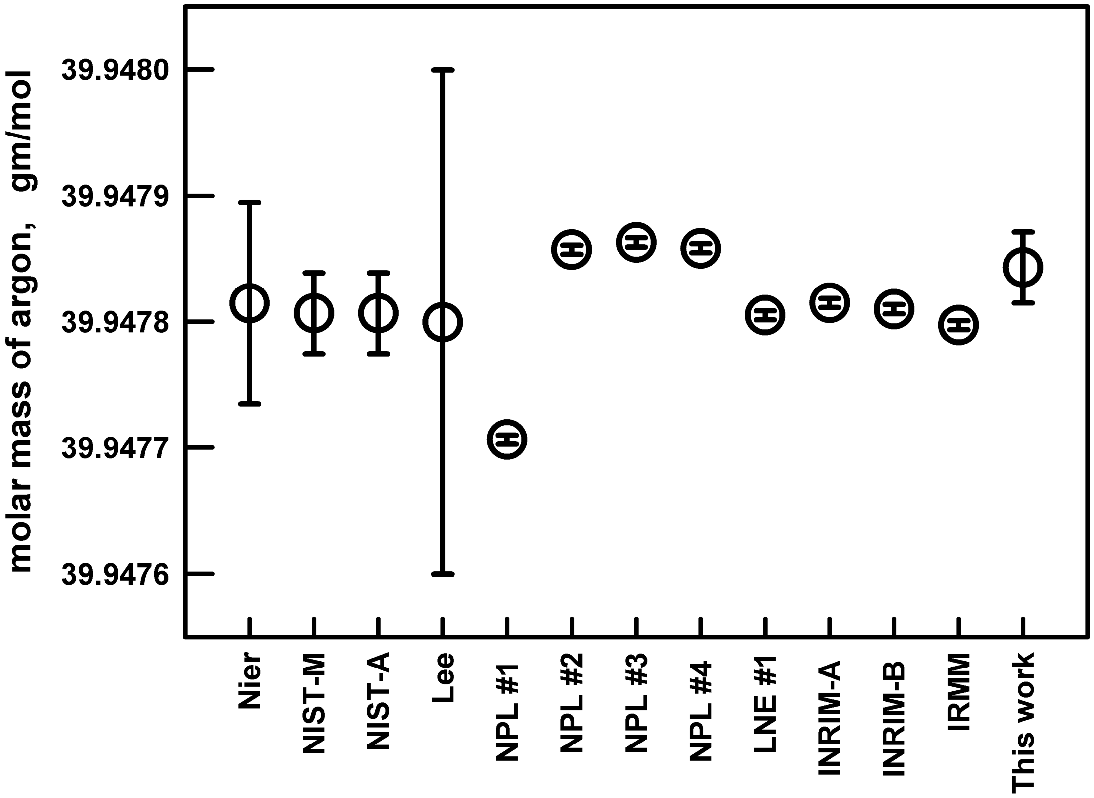

Fig. 4. Values of M_{Ar} for argon from 13 commercial samples. The data sources are: Nier [31]; NIST-A and NIST-B [3]; all others [29], except for "This work".

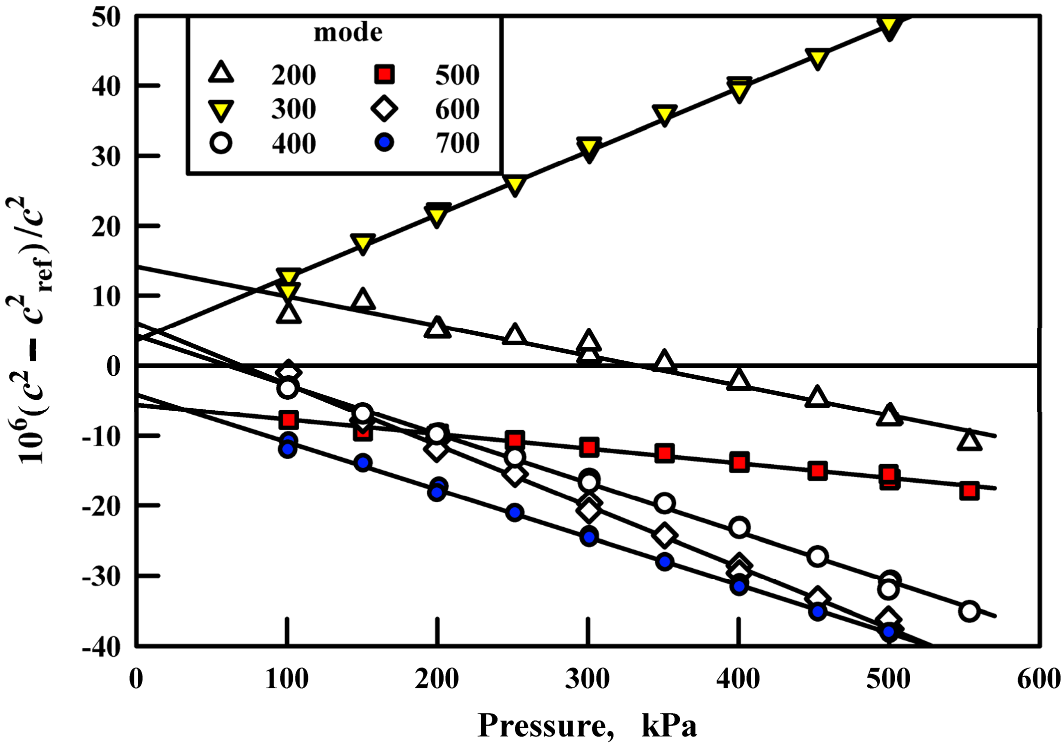

Fig. 5. Present values of the square of the speed of sound in argon at T_{TPW} determined with modes l = 2, . . .,7, compared with results of Moldover *et al*. [3]

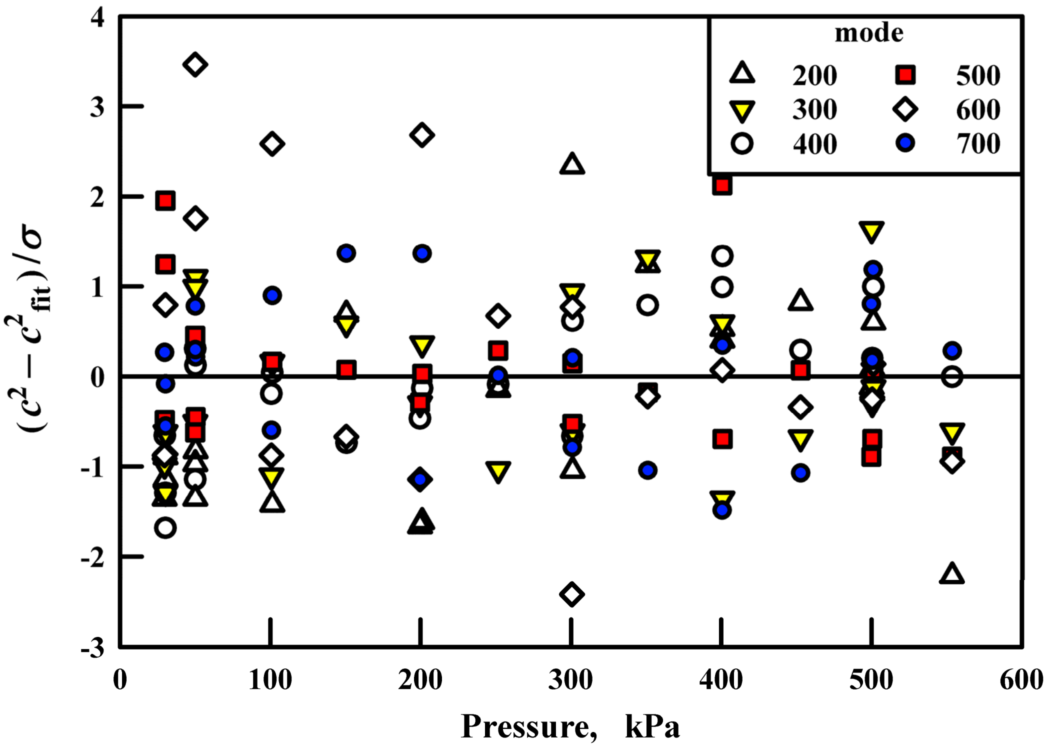

Fig. 6. Deviations of the speed-of-sound data from the surface fit divided by twice the uncertainty of a frequency measurement from Eq. (25).

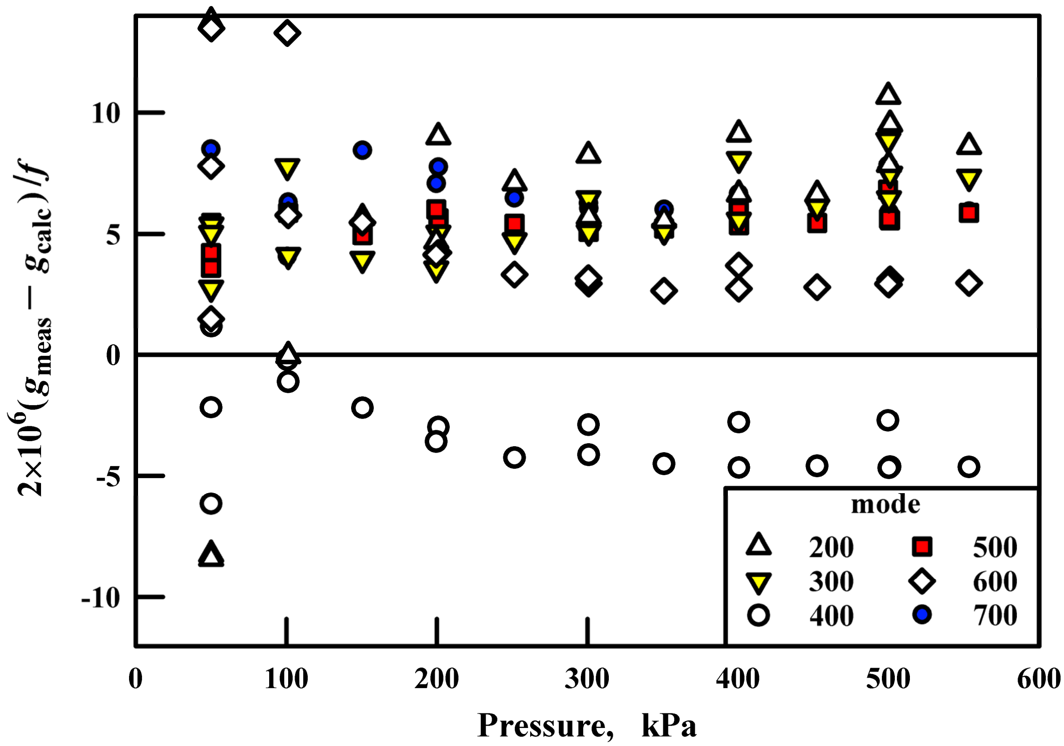

Fig. 7. Mode-dependent excess half-widths multiplied by 2×10^6/frequency.

References

1 Mills I M, Mohr P J, Quinn T J, Taylor B N and Williams E R., 2006 *Metrologia* **43** 227-46

2 Colclough A R, Quinn T J, and Chandler T R D 1979 *Proc. R. Soc. Lond.* **A368** 125-39

3 Moldover M R, Trusler J P M, Edwards T J, Mehl J B, and Davis R S 1988 *J. Res. Natl. Bur. Stand.* **93** 85-144

4 Pitre L, Gruianvarch C, Sparasci F, Guillou A, Truong D, Hermier Y and Himbert M E 2009 *C. R. Phys.* **10** 835-48.

5 Gavioso R M, Benedetto G, Albo P A G, Ripa D M, Merlone A, Guianvarc'h C, Moro F and Cuccaro R 2010 *Metrologia* **47** 387-409.

6 Pitre L, Sparasci F, Guillou A, Truong D, Hermier Y, Himbert M E 2010 New determination of the Boltzmann constant with an acoustic method *Conference on Precision Electromagnetic Measurements* (Korea, Daejeon, 13-18 June, 2010).

7 Sutton G, Underwood R, Pitre L, Podesta M de and Valkiers S 2010 *Int. J. Thermophys.* **31** 1310-46.

8 Segovia J J, Maza D V, Martin M C, Gomez E, Tabacaru C and Campo D del 2010 *Int. J. Thermophys.* **31** 1294-1309.

9 Zhang J T, Lin H, Sun J P, Feng X J, Gillis K A, Moldover M R 2010 *Int. J. Thermophys.* **31** 1273-1293.

10 Moldover M R, Boyes S J, Meyer C W, and Goodwin A R H 1999 *J. Res. Natl. Inst. Stand. Technol.* **104** 11-46

11 Ewing M, B and Trusler J P M 2000 *J.Chem.Thermodynam.* **321**, 229–55

12 Benedetto G, Gavioso R M, Spagnolo R, Marcarino P and Merlone A 2004 *Metrologia* **41** 74-98

13 Pitre L, Moldover M R, and Tew W L 2006 *Metrologia* **43** 142-62

14 Ripple D C, Strouse G F, and Moldover M R 2007 *Int. J. Thermophys.* **28** 1789-99.

15 Gillis K A, Lin H and Moldover M R 2009 *J. Res. Natl. Inst. Stand. Technol*. **114** 263-285.

16 Lin H, Gillis K A and Zhang J T 2010 *Int. J. Thermophys.* **31** 1234-1247.

17 Zhang J T, Lin H, Sun J P, Feng X J, Gillis K A, Moldover M R 2010 Re-determination of the Boltzmann constant with fixed path cylinders *Presented on TEMPMEKO & ISHM 2010* (Slovenia, Portoroz, 31 May-4 June).

18 Mohr P J, Taylor B N and Newell D B 2008 *Rev. Mod. Phys.* **80** 633-729.

19 Ewing M B, McGlashan M L and Trusler J P M 1986 *Metrologia* **22** 93-102.

20 Moldover M R and Trusler J P M 1988 *Metrologia* **25** 165-187.

21 Ewing M B, Owusu A A and Trusler J P M 1989 *Phys. A* **156** 899-908.

22 Ewing M B and Goodwin A R H 1992 *J. Chem. Thermodyn.* **24** 531-47.

23 Dittman, S, Lindenau, B E, and Tilford, C R, 1989, J. Vac. Sci. Technol. A7, 3356.

24 Mehl J. B., Moldover M. R. and Pitre L., 2004, *Metrologia* **41** 295-304.

25 Palik E D1985 *Handbook of Optical Constants of Solids* (New York: Academic) .

26 Barakat N, Mokhtar S and Haadi K A 1964 *J. Opt. Soc. Am.* **54** 213-216.

27 Peck E R and Fisher D J 1964 *J. Opt. Soc. Am.* **54** 1362-1364.

28 Tilford C F 1977 *Applied Optics* **16** 1857

29 Valkiers, S., Vendelbo, D., Berglund, M, de Podesta, M. 2010, Int. J. Mass Spectrometry, 291, 41.

30 Pitre L, Guillou A, Truong D, Sparasci F and Guianvarc'h C 2009 An acoustic/microwave determination of the Boltzmann constant at LNE-INM/CNAM Presented at *The IV Int. Workshop on Progress in Determining the Boltzmann Constant* (Torino, Italy, 22–24 September 2009)

31 Nier A O, 1950 *Phys. Rev.* **77** 789-93.

32 Lee J Y, Marti K, Severinghaus J P, Kawamur K, Yoo H S, Lee J B, Kim J S 2006 *Geochimica et Cosmochimica Acta* **70** 4507-12

33 Gillis, K. A., Shinder, I. I., and Moldover, M. R., "Thermoacoustic Boundary Layers Near the Liquid-Vapor Critical Point", Phys. Rev. E., Vol **70**, 021201 (2004).

34 Moldover, M. R. "Optimizing Acoustic Measurements of the Boltzmann Constant", Comptes Rendus Physique, **10**, 815-827 (2009).

35 Goodwin, A R H, *Thermophysical Properties from the Speed of Sound*, Ph.D. Thesis, University of London (1988).

36 Wieser, M. E.; Berglund, M., “Atomic weights of the elements 2007 (IUPAC Technical Report), Pure Appl. Chem. 2009, 81(11), 2131-2156.

37 Laeter, J.R.; Bohlke, J.K.; De Bievre, P.; Hidaka, H.; Peiser, H.S.; Rosman, K.J.R.; Taylor, P.D.P., “Atomic weights of the elements: Review 2000” (IUPAC Technical Report) 2003, Pure Appl. Chem., 75(6), 683-800.